Applications of the Radon transform, Stratigraphic filtering, and Object-based stochastic reservoir modeling

Ethan J. Nowak

Dissertation submitted to the Faculty of the
Virginia Polytechnic Institute and State University
in partial fulfillment of the requirements for the degree of

Doctor of Philosophy
in
Geosciences

Matthias G. Imhof, Chair
James W. Castle
Cahit Coruh
Matthew Mikulich
J. Arthur Snoke

September 22, 2004
Blacksburg, VA

Keywords: Radon transform, Frequency filtering,
Inversion, Signal processing, Reservoir modeling

Applications of the Radon transform, Stratigraphic filtering, and Object-based stochastic reservoir modeling

Ethan J. Nowak

Abstract

The focus of this research is to develop and extend the application of existing technologies to enhance seismic reservoir characterization. The chapters presented in this dissertation constitute five individual studies consisting of three applications of the Radon transform, one aspect of acoustic wave propagation, and a pilot study of generating a stochastic reservoir model.

The first three studies focus on the use of the Radon transform to enhance surface-recorded, controlled-source seismic data. First, the use of this transform was extended to enhance diffraction patterns, which may be indicative of subsurface fractures. The geometry of primary reflections and diffractions on synthetic common-shot-gather data indicate that Radon filters can predict and model primary reflections upon inverse transformation. These modeled primaries can then be adaptively subtracted from the input gather to enhance the diffractions. Second, I examine the amplitude distortions at near and far offsets caused by free-surface multiple removal using Radon filters. These amplitudes are often needlessly reduced due to a truncation effect when the commonly used, unweighted least-squares solution is applied. Synthetic examples indicate that a weighted solution to the transformation minimizes this effect and preserves the reflection amplitudes. Third, a novel processing flow was developed to generate a stacked seismic section using the Radon transform. This procedure has the advantage over traditional summation of normal moveout corrected common midpoint gathers because it circumvents the need to perform manual and interpretive velocity analysis.

The fourth study involves the detection of thin layers in periodic layerstacks. Numerical modeling of acoustic wave propagation suggests that the sinusoidal components of an incident signal with a wavelength that corresponds to the periodicity of the material be preferentially reflected. Isolating the different portions of the reflected wavefield and calculating the energy spectra may provide evidence of thin periodic layers which are deterministically unresolvable on their own.

Object-based reservoir modeling often incorporates the use of lithology logs, deterministic seismic interpretation, architectural element analysis, geologic intuition, and modern and outcrop analogs. This last project consists of a pilot study where a more quantitative approach to define the statistical parameters currently derived through geologic intuition and analogs was developed. This approach utilizes a simulated annealing optimization technique for inversion and the pilot study shows that it can improve the correlation between synthesized and control logs.

Acknowledgments

My sincerest appreciation is extended to Matthias Imhof for his guidance and patience with so many seemingly unrelated studies. I would also like to thank the members of my research advising committee consisting of James Castle, Martin Chapman, Cahit Coruh, Matt Mikulich, and Arthur Snoke for their assistance in the presented works.

I also owe a special thanks to John Constain and Cahit Coruh.

I would like thank ConocoPhillips Company for allowing the publication of the study on amplitude preservation after Radon filtering multiples; in particular Philip Anno, Douglas Foster, F. David Lane, and Charles Mosher for their advice and help.

I would also like to thank ChevronTexaco Production Company in Bakersfield, California for supplying the data and allowing me to publish the results of the object-based stochastic facies inversion study; Roxar for use of the RMS software package; and the Department of Energy for funding the project under contract DE-FC26-00BC15301.

...and of course my loving wife Stephanie and beautiful baby girl Amelia.

Contents

1 Introduction **1**

2 Diffractor signature enhancement via weighted and unweighted Radon transforms **4**

2.1 Introduction 4

2.2 Filtering process 5

2.3 Results 8

2.4 Conclusion 11

3 Amplitude preservation after Radon filtering multiples **12**

3.1 Introduction 12

3.2 Radon filtering 13

3.3 Prewhitening 14

3.4 Random noise 16

3.5 Amplitude preservation 17

3.6 Conclusion 21

4 Stacking seismic data without velocity analysis **22**

4.1 Introduction 22

4.2 Stacking processes 23

4.3 Application to field data 25

4.4 Conclusion 26

5 Stratigraphic filtering **29**

5.1 Introduction 29

5.2 Bragg scattering 30

5.3 Frequency filtering in periodic layerstacks 32

Analytical solution 33

Numerical solution 35

5.4 Discussion 36

5.5 Conclusion 41

6 Object-based stochastic facies inversion **43**

6.1 Introduction 43

6.2 Process 45

6.3 Application to the Coalinga heavy oil field 48

6.4 Discussion and Conclusions 54

A Radon Transform **58**

B Summary of calculations **61**

Bibliography **63**

List of Figures

2.1 Filtering primary reflections on raw CSG's with the weighted hyperbolic Radon transform 7

2.2 Filtering primary reflections on raw CSG's with the unweighted hyperbolic Radon transform 8

2.3 Filtering primary reflections on NMO corrected CSG's with the weighted hyperbolic Radon transform 9

2.4 Results of Radon filtering NMO corrected primary reflections 10

3.1 Filtering multiples with the weighted hyperbolic Radon transform 14

3.2 Filtering multiples with the unweighted hyperbolic Radon transform 15

3.3 L_2-norm curves resulting from filtering multiples 16

3.4 The effect of random noise on the filtering process 17

3.5 Near and far offset artifacts in the Radon domain 18

3.6 Portion of an NMO corrected synthetic CMP gather exhibiting the additive contamination of water bottom multiples on reflections. 19

3.7 AVO plots after filtering multiples with the various Radon transforms. 20

4.1 NMO and Radon stacking techniques 24

4.2 Results of NMO and Radon stacking offshore field data 25

4.3 Nigeria Radon transform pair 27

4.4 Subsets of the NMO and Radon stacking offshore field data 28

5.1 1-D Bragg scattering model of nodes 30

5.2 1-D stratigraphic filtering model of nodes 32

5.3 Energy spectra for reflection and transmission coefficients. 34

5.4 Velocity model and reflected wavefield for a periodic layerstack. 36

5.5 Reflected energy spectra resulting from a periodic layerstack. 37

5.6 Energy spectra for the entire reflected and transmitted wavefields and the incident signal. 38

5.7 Fourier transform pairs depicting the filtering process. 39

5.8 Cross-plot showing mean frequency as a function of varying layer thicknesses. 40

5.9 Cross-plot showing varying layer thicknesses as a function of bandwidth. . . 41

5.10 Examples of thin and thick layers establishing a 70 Hz binary material. . . . 42

6.1 Schematic depicting the object-based stochastic facies inversion. 46

6.2 Location of the Coalinga oil field in southwestern California. 49

6.3 Coalinga study site 49

6.4 Dominant stratigraphic intervals within the Temblor formation 50

6.5 Convergence of the inversion (correlation verses iteration) from 32% to 51% in nine iterations. 54

6.6 Cross-section, through the initial and final realizations, intersecting three control wells 55

6.7 Enlarged view of the control and extracted interval facies logs. 56

A.1 Radon transform pairs 59

List of Tables

2.1 Efficiency of Radon filters applied in different domains. 10

6.1 Parameters and ranges for the basal zone of the Temblor formation. 51

6.2 Parameters used to generate a realization for the basal zone of the Temblor formation with 51% agreement. 53

Chapter 1

Introduction

The focus of this research is to develop and extend the application of existing technologies to enhance seismic reservoir characterizations. The chapters presented in this dissertation constitute five individual studies consisting of three applications of the Radon transform, one theoretical study of acoustic wave propagation, and a pilot study of generating a stochastic reservoir model.

The first application of the Radon transform focuses on enhancing diffraction patterns in surface recorded seismic data by filtering primary reflections. Bansal and Imhof (2004) first introduced this application of the transform. The results were usable, but they felt that advanced Radon transforms would perform even better. The results of my modified processing flow, presented in Chapter 2, indicate that the Radon transform can successfully enhance diffraction patterns by removing primary reflections when applied to offset recorded synthetic seismic data.

The second application deals with the most common application of the Radon transform, which is to suppress water bottom and interbed multiples from normal moveout corrected common midpoint gathers. Typically, unweighted solutions to the transform needlessly reduce reflector amplitudes at near and far offsets thus diminishing their diagnostic value.

The advent of weighted solutions to the transform have minimized this effect, however other advantages of using these solutions have not been reported. Therefore, in Chapter 3, the advantages of using the weighted least-squares solution to the transform when suppressing multiple reflections are presented. These advantages include ease of selecting a prewhitening factor, reduced sensitivity to random noise, and reflector amplitude preservation.

Thirdly, a means to stack seismic data without performing velocity analysis was developed. This technique, described in Chapter 4, utilizes the Radon transform and has an advantage over summing normal moveout corrected common midpoint gathers because it does not require a velocity model. Circumventing the need for velocity analysis to produce a stacked seismic section or volume reduces the man hours required to process surface recorded seismic data and does not introduce interpreter bias.

Chapter 5 deals with the question, "What can be said about thin layers that can not be resolved by a reflection?" Numerical modeling of acoustic wave propagation suggests that the sinusoidal components of an incident signal with a wavelength that corresponds to the periodicity of the material be preferentially reflected. Based on this discovery, by isolating different portions of the reflected wavefield the calculated energy spectra can provide evidence of thin periodic layers which are deterministically unresolvable on their own.

Chapter 6 contains a pilot study on object-based reservoir modeling. Such models often incorporate the use of lithology logs, deterministic seismic interpretation, architectural element analysis, geologic intuition, and modern and outcrop analogs to generate a realization of a reservoir. The geologic intuition and analogs often define the statistical parameters that dictate the internal composition and structure of the reservoir model. Because a more quantitative approach to define these parameters may improve the correlation between the model and observed data, a simulated annealing guided search technique was chosen as a proxy to intuition and analogs. The preliminary results of this pilot study suggest that by including an inversion scheme to optimize the parameters necessary to generate a reservoir

model, it is possible to improve the correlation between synthesized and control logs.

The included appendices provide descriptions and calculations common to one or more chapters in this dissertation. The theory and derivation of the forward and inverse Radon transform is included in Appendix A, and a summary of various time domain and frequency domain calculations is provided in Appendix B.

Chapter 2

Diffractor signature enhancement via weighted and unweighted Radon transforms

2.1 Introduction

Secondary porosity, in the form of fractures, may be a target when drilling production wells in hydrocarbon reservoirs. Numerical models of waves recorded at offsets suggest that fracture events may resemble diffractions (e.g., Daley et al., 2002; Saenger et al., 2002). These events can be enhanced by removal of reflections and other predictable events. Local scatterers embedded in a uniform medium produce hyperbolic events, where the apeces of these hyperbolas coincide with the location of the scatterers on common shot gather (CSG) data. In order to accentuate these diffraction signatures, primary and multiple reflections need to be removed.

In principle, the Radon transform has the ability to sum events exhibiting a linear, parabolic or hyperbolic trajectory in the space-time domain to a single event in the trans-

formed domain. As a result of this, Radon filtering has been a resounding success in suppressing multiple reflections from normal moveout (NMO) corrected seismic data (Foster and Mosher, 1992; Trad et al., 2003).

The purpose of this study is to develop a means to enhance diffractions, observed in seismic data, by suppressing primary reflections. The use of Radon filters to accomplish this objective, first introduced by Bansal and Imhof (2004), has shown promise because primary reflections are focusable by the Radon transform. Raw CSG reflections are hyperbolic with apeces near zero offset, or nearly flat after NMO correction. These events are focused to a localized event in the Radon domain, whereas the energy associated with a scatterer is smeared in the transform domain. This allows for design of Radon filters that remove much of the energy associated with the scatterers, thus successfully modeling the reflections upon inverse transformation. The modeled reflections are then adaptively subtracted from the original data to emphasize diffraction signals.

This filtering technique is applied to synthetic CSG and NMO corrected CSG data, generated by the space-time finite-difference approximation to the acoustic wave equation (e.g., Jensen et al., 1994) described in Equation B.5 in Appendix B. We chose a weighted and unweighted damped least-squares solution to the linear, parabolic and hyperbolic Radon transform of Herrmann et al. (2000) to suppress the reflections on the synthetic NMO corrected CSG data and a weighted and unweighted hyperbolic transform of Herrmann et al. (2000) to filter reflections from raw synthetic CSG data.

2.2 Filtering process

To illustrate the filtering process acting on raw CSG data, consider the two processing flows depicted in Figures 2.1 and 2.2. These two flows utilize the weighted and unweighted Radon transforms described in Appendix A. Here the common shot gather $F(x,t)$ consists of five

local scatterers embedded in the uniform medium between the primary reflections at 1.0 and 1.125 seconds (two-way traveltime). As can be seen on Figures 2.1(b) and 2.2(a), the two primary reflections focus in the hyperbolic Radon domain into two localized events at their respective moveout and intercept times, whereas the energy associated with the diffractions is smeared across the transform domain. By filtering the negative, small and very large moveouts (Figure 2.1(c)), much of the energy associated with the diffractions is removed after inverse transformation, as shown on Figures 2.1(d) and 2.2(b). These modeled primaries $H(x,t)$ are then adaptively subtracted, $F(x,t) - \ell H(x,t)$ where ℓ is a small scalar chosen by trial and error such that it produces the min[abs($F(x,t) - \ell H(x,t)$)], from the original data to yield the diffractions depicted in Figures 2.1(e) and 2.2(c). The desired outcome of the filtering process, shown on Figure 2.1(f), consists solely of the five diffractions produced by the scatterers.

A similar processing flow, depicted in Figure 2.3, can be applied to the CSG data shown on Figure 2.1(a) after undergoing the correction for normal moveout $F(x,t)$, shown on Figure 2.3(a). Here the horizontal reflectors at 1.0 and 1.125 seconds are localized at zero moveout and their respective zero offset traveltimes, whereas the skewed hyperbolic events, associated with the scatterers are smeared in the transform domain depicted on Figure 2.3(b). The horizontal reflectors $H(x,t)$, shown on Figure 2.3(d), are modeled upon inverse transformation of the Radon domain after applying a boxcar filter centered at zero moveout (Figure 2.3(c)). These modeled reflectors are, however, accompanied by two horizontal artifacts located at 1.05 and 1.075 seconds. To suppress the imprint of these artifacts on the filtered data, while removing the primary reflections, a unique factor ℓ is determined for each traveltime during the adaptive subtraction. For instance, $F(x,t) - \ell_t H(x,t)$ where ℓ_t is a time-variant and offset-constant small scalar chosen to produce the min[abs($F(x,t) - \ell_t H(x,t)$)]. This allows an optimum factor ℓ_t to be chosen at a time sample corresponding to a primary reflection and a near zero factor at time samples corresponding to the artifacts. The result of this process is displayed on Figure 2.3(e) and for comparison the desired outcome,

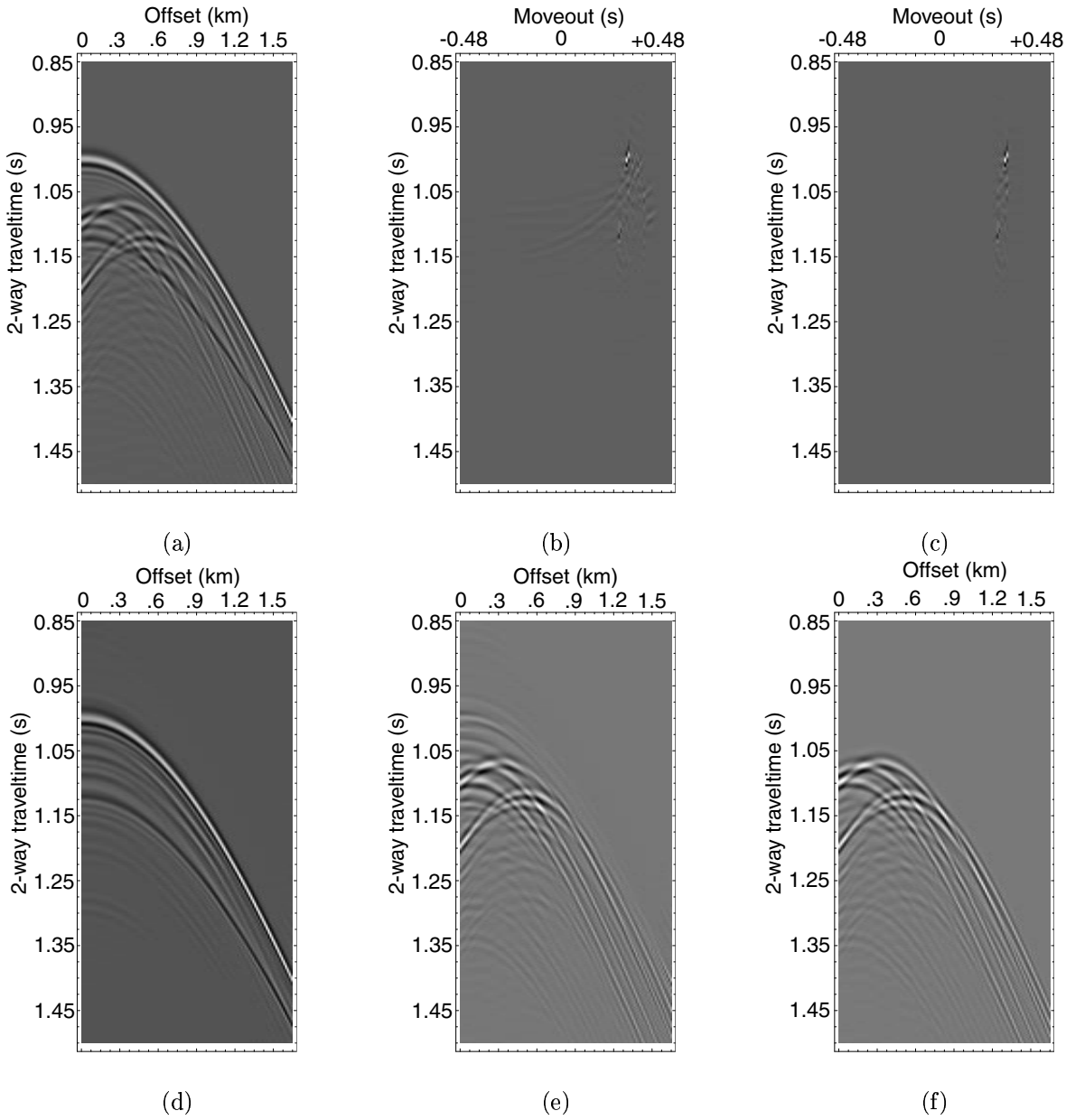

Figure 2.1: Illustrates the filtering process from **(a)** the input raw CSG data; **(b)** the weighted hyperbolic Radon transform of **(a)**; **(c)** after filtering negative, small and very large moveouts; **(d)** the inverse transform of **(c)**; **(e)** the filtered data; and **(f)** the desired outcome.

consisting of the five diffractions, is shown on Figure 2.3(f).

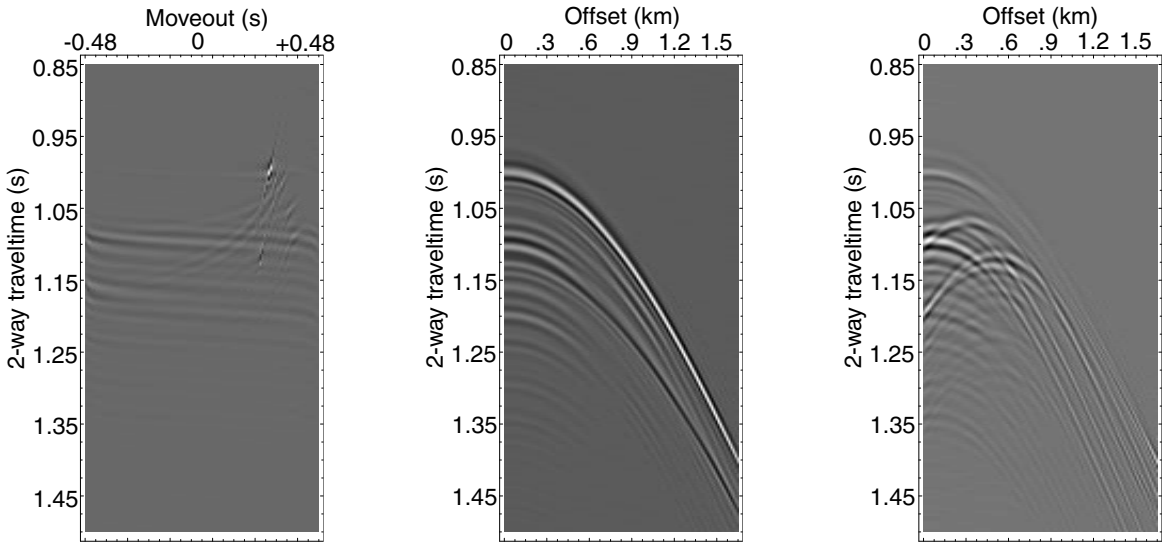

(a) (b) (c)

Figure 2.2: Illustrates the same filtering process shown in Figure 2.1 using (a) the unweighted hyperbolic Radon transform of 2.1(a); (b) the inverse transformation after filtering negative and small moveouts; and (c) the filtered data

2.3 Results

The suitability of these various Radon filters to suppress primary reflections is quantified by a normalized crosscorrelation function. This function

$$E = \frac{1}{x_{max}} \sum_{1}^{x_{max}} \frac{2 \sum_{\omega_{min}}^{\omega_{max}} R(x,\omega) S^*(x,\omega)}{\sum_{\omega_{min}}^{\omega_{max}} R(x,\omega) R^*(x,\omega) + \sum_{\omega_{min}}^{\omega_{max}} S(x,\omega) S^*(x,\omega)}, \tag{2.1}$$

modified from Sen and Stoffa (1991), where * denotes complex conjugate, is a useful metric for assessing the match between a desired outcome $R(x,t)$ and an actual outcome $S(x,t)$. For this case the actual outcome is the result of applying the weighted linear, parabolic and hyperbolic and unweighted linear Radon filter to the NMO corrected CSG data, which are shown on Figures 2.4(a), 2.4(b), 2.3(e), and 2.4(c), and the desired outcome is the five diffractions shown on Figure 2.3(f).

The results of applying the various Radon filters are listed in Table 2.1. Based on these

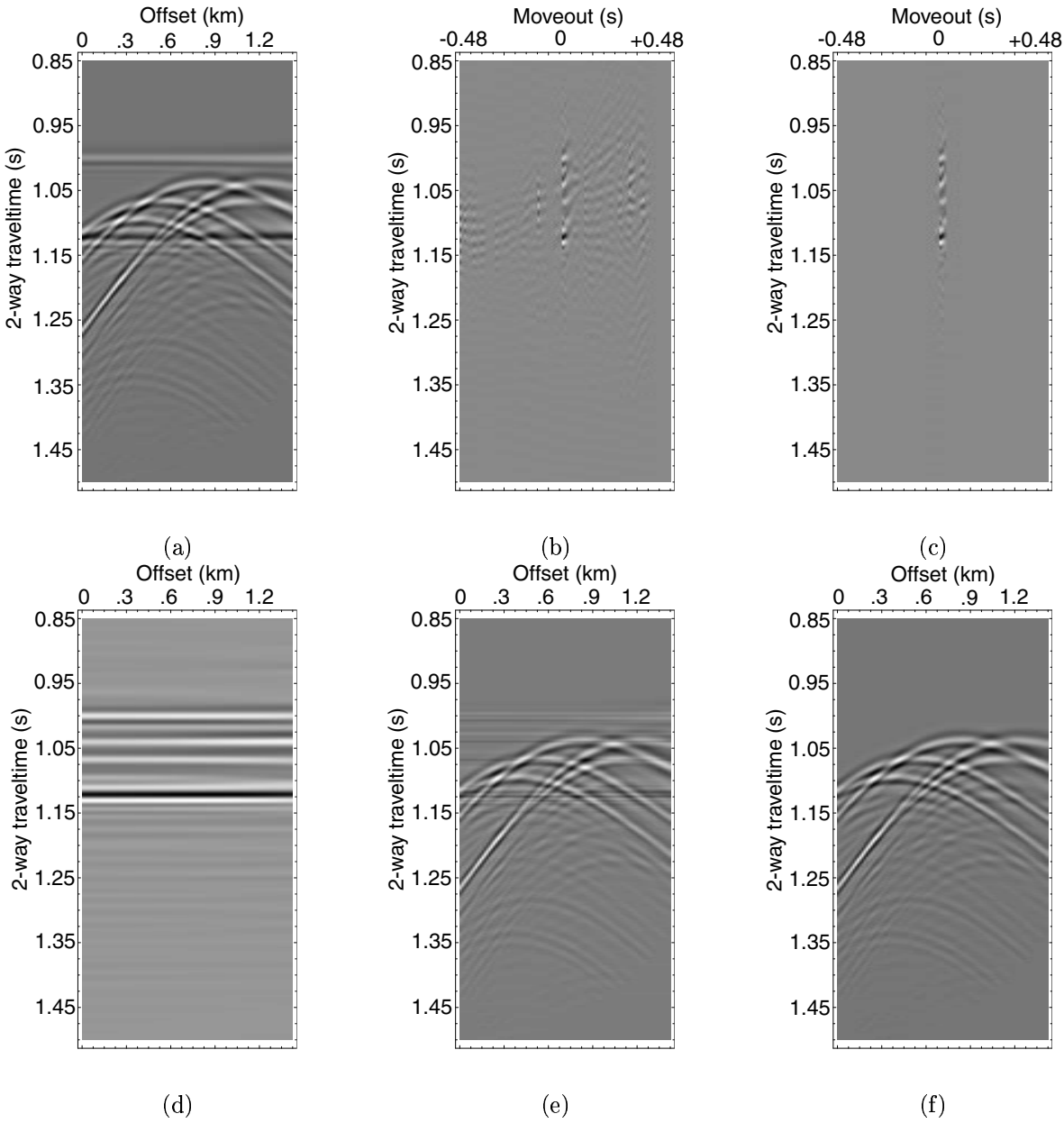

Figure 2.3: Illustrates the filtering process from **(a)** the CSG data depicted in Figure 2.1(a) after NMO correction; **(b)** the weighted hyperbolic Radon transform of **(a)**; **(c)** after applying a boxcar filter centered at zero moveout; **(d)** the inverse transform of **(c)**; **(e)** the filtered NMO corrected data; and **(f)** the desired outcome.

synthetic experiments, a marketable improvement occurs when the Radon filters operate on common shot gathers that have been corrected for normal moveout with 92% crosscorrelation versus 34% crosscorrelation when the filter is acting on raw CSG data. These experiments

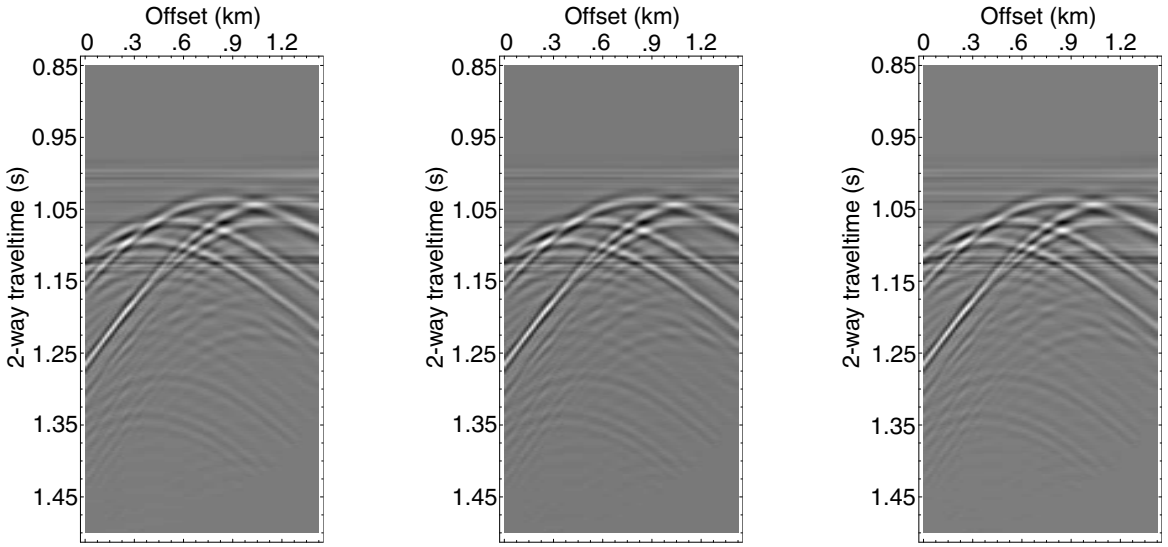

(a) (b) (c)

Figure 2.4: Depicting the results of applying **(a)** the weighted linear; **(b)** the weighted parabolic; and **(c)** the unweighted linear Radon filters to the NMO corrected CSG data shown on Figure 2.3(a).

also indicate that there is no distinct advantage to using the weighted solution to the Radon transform to filter primary reflections on NMO corrected CSG data.

Table 2.1: Efficiency of Radon filters applied in different domains.

Input Data	Radon Filter Type	Crosscorrelation
NMO corrected CSG	Weighted Linear	0.9279
NMO corrected CSG	Weighted Parabolic	0.9250
NMO corrected CSG	Weighted Hyperbolic	0.9336
NMO corrected CSG	Unweighted Linear	0.9240
Raw CSG	Weighted Hyperbolic	0.3212
Raw CSG	Unweighted Hyperbolic	0.3480

2.4 Conclusion

The use of Radon transforms was extended to suppress primary reflections for the purpose of enhancing diffraction patterns in common shot gathers. In addition, the filters could also be used to enhance reflections and suppress diffractions and noise. The filters, designed from the linear, parabolic and hyperbolic Radon transform, were applied to normal moveout corrected common shot gathers, whereas only the hyperbolic filter was applied to the raw common shot gather data. Based on the normalized crosscorrelation between the desired outcome and the filtered data, these synthetic examples indicate that filters operating on normal moveout corrected common shot gathers outperform those operating on raw common shot gather data. Specifically, when the filters were designed and applied after NMO correction, 92 to 93% of the desired outcome was achieved whereas a 32 to 34% match was attained when the filters were designed and applied prior to correcting for normal moveout. Based on these NMO corrected synthetic experiments, filters acting on an unweighted solution to the linear Radon transform performed as well as those operating from any of the weighted solutions to the transform.

Chapter 3

Amplitude preservation after Radon filtering multiples

3.1 Introduction

Using the Radon transform to suppress multiple reflections plays an intricate role in seismic data processing and continues to receive much attention in the literature (Foster and Mosher, 1992; Bickel, 2000; Herrmann et al., 2000; Trad et al., 2003). In principle, the Radon transform is a quasi-reversible transformation which has the ability to sum events exhibiting a linear, parabolic or hyperbolic trajectory in one domain to a single event in the transform domain. As a result, filters are designed in the Radon domain to remove much of the energy associated with primary reflections leaving behind the multiples. This operation is performed on normal moveout (NMO) corrected common midpoint (CMP) gathers in order to distinguish between the primary and multiple reflections. Upon inverse transformation of the filtered Radon domain, the multiple reflections are modeled and adaptively subtracted from the CMP gather.

The purpose of this study is to examine the amplitude-preserving advantage of using

the weighted least-squares solution (e.g., Herrmann et al., 2000) to the linear, parabolic, and hyperbolic Radon transform over the unweighted solution for suppressing multiple reflections. These filtering techniques were applied to synthetic CMP gathers and the issue of choosing an appropriate prewhitening factor and the sensitivity to random noise between the two filtering techniques is addressed. The synthetic seismic data was generated by the space-time finite-difference approximation to the acoustic wave equation (e.g., Jensen et al., 1994) outlined in Equations B.1-B.5 in Appendix B.

3.2 Radon filtering

To illustrate a similar filtering process as described in Chapter 2, Figure 2.1, using the Radon transforms described in Appendix A, consider the model depicted in both Figures 3.1(a) and 3.2(a). These models consists of three hyperbolic events located at t_a, t_b and t_c and two horizontal events located at t_b and t_c. Note the horizontal event at t_b exhibits a Type 1 (Verm and Hilterman, 1995) AVO anomaly, decreasing amplitude variation with offset. Figures 3.1(b) and 3.2(b) depict the weighted and unweighted hyperbolic Radon representation of Figures 3.1(a) and 3.2(a). In this domain, the horizontal reflections are localized at zero moveout and their respective zero offset traveltimes t_b and t_c, whereas the hyperbolic events are focused at their respective moveout and travel times t_a, t_b and t_c. Upon removing the events located at zero and negative moveouts, the inverse transform models the hyperbolic events shown on Figures 3.1(c) and 3.2(c), which are adaptively subtracted to illuminate the horizontal reflections shown on Figures 3.1(d) and 3.2(d).

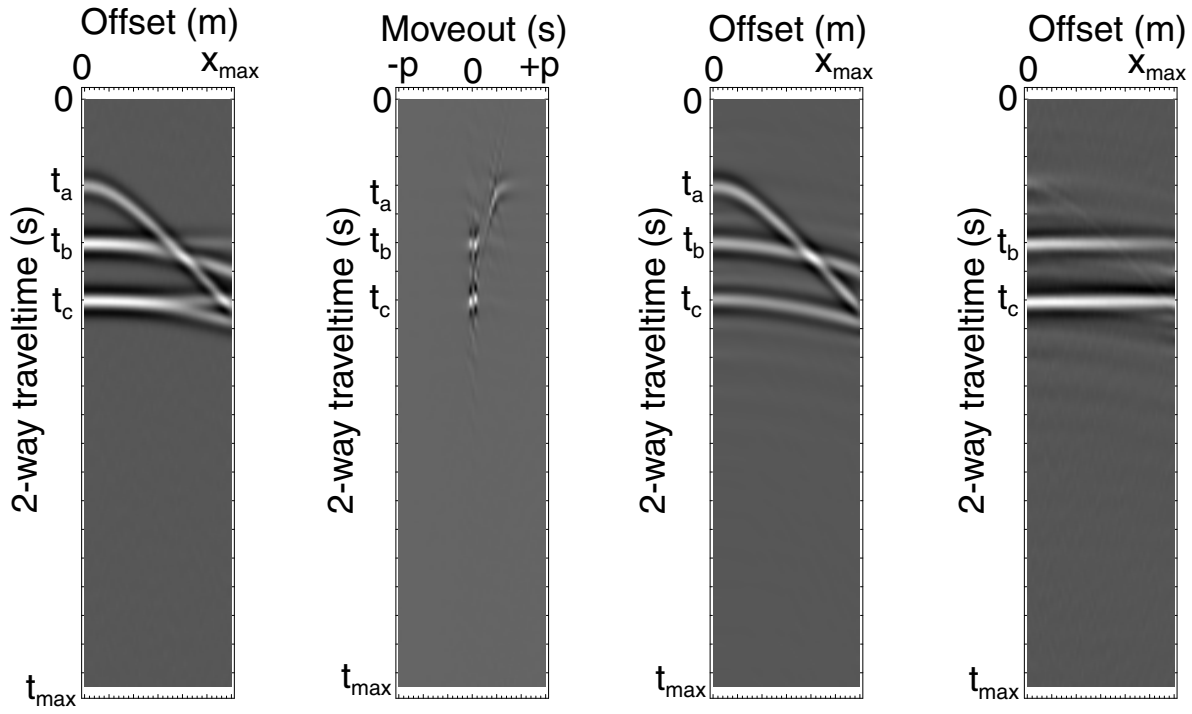

(a) (b) (c) (d)

Figure 3.1: Illustrates the filtering process from **(a)** the input, **(b)** the weighted hyperbolic Radon transform of **(a)**, **(c)** the inverse transform of **(b)** after negative and zero moveouts removed, and **(d)** the filtered data, **(a)-(c)**.

3.3 Prewhitening

In order to address the parameterization of the prewhitening factor, the above process is systematically repeated for various values of the prewhitening factor α (Appendix A). The results are shown on Figure 3.3 for weighted and unweighted solutions to the linear, parabolic and hyperbolic transforms as L_2-norm curves plotting the data misfit versus model size.

In this example, the L_2-norm of the misfit is defined as $(\sum_i |d_i - G_{ij}m_j|^2)^{\frac{1}{2}}$ where $G_{ij}m_j$ is the filtered data and d_i is the desired outcome, or, in this case, the original data without the hyperbolic events. The model size, defined as $(\sum_i |m_i|^2)^{\frac{1}{2}}$, is calculated from the resultant forward transform of the original data to ensure a parsimonious Radon domain. For each test,

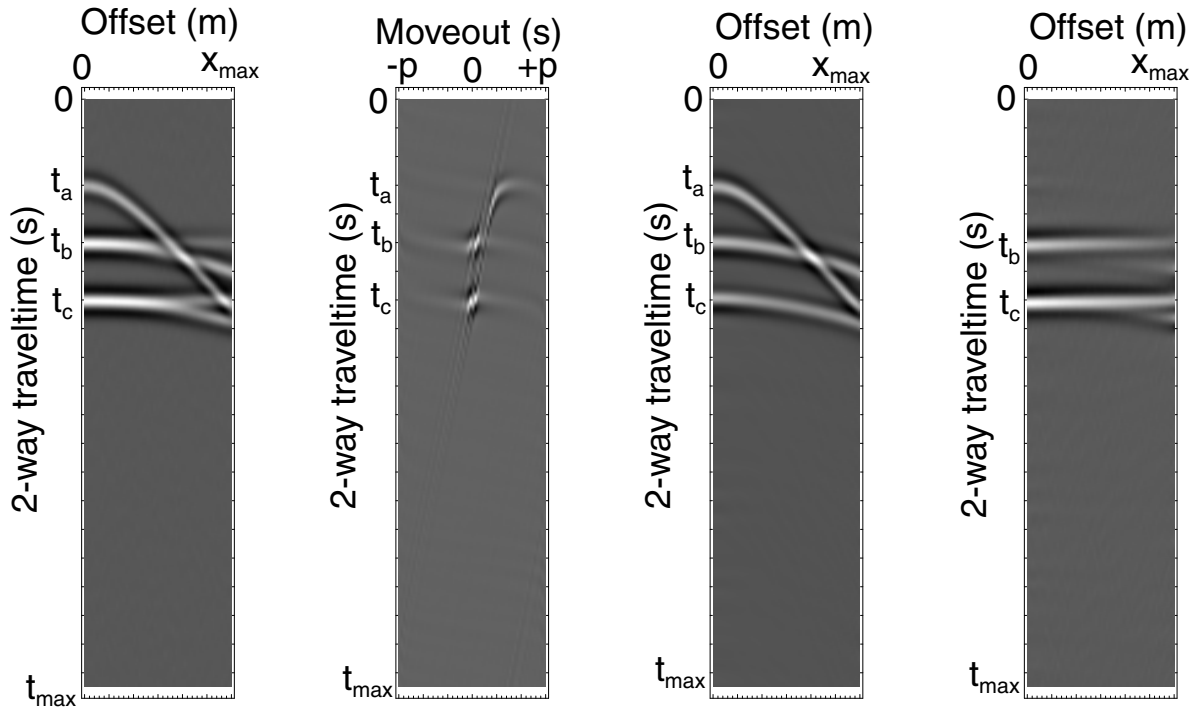

(a) (b) (c) (d)

Figure 3.2: Illustrates the filtering process from **(a)** the input, **(b)** the unweighted hyperbolic Radon transform of **(a)**, **(c)** the inverse transform of **(b)** after negative and zero moveouts removed, and **(d)** the filtered data, **(a)-(c)**.

the unweighted solutions yield a typical L_2-norm curve where values for α would be chosen to simultaneously minimize the misfit and model size (i.e. $\alpha \approx 0.001$, 0.0001 and 0.0001 for the linear, parabolic and hyperbolic transforms). However when the weighted solutions were applied, the model size and misfit were minimized regardless of the chosen prewhitening factor. This suggests that the weighted transform is less sensitive to the prewhitening factor than the unweighted one, and hence, less tuning is required in choosing the prewhitening factor for the weighted solution than the unweighted one.

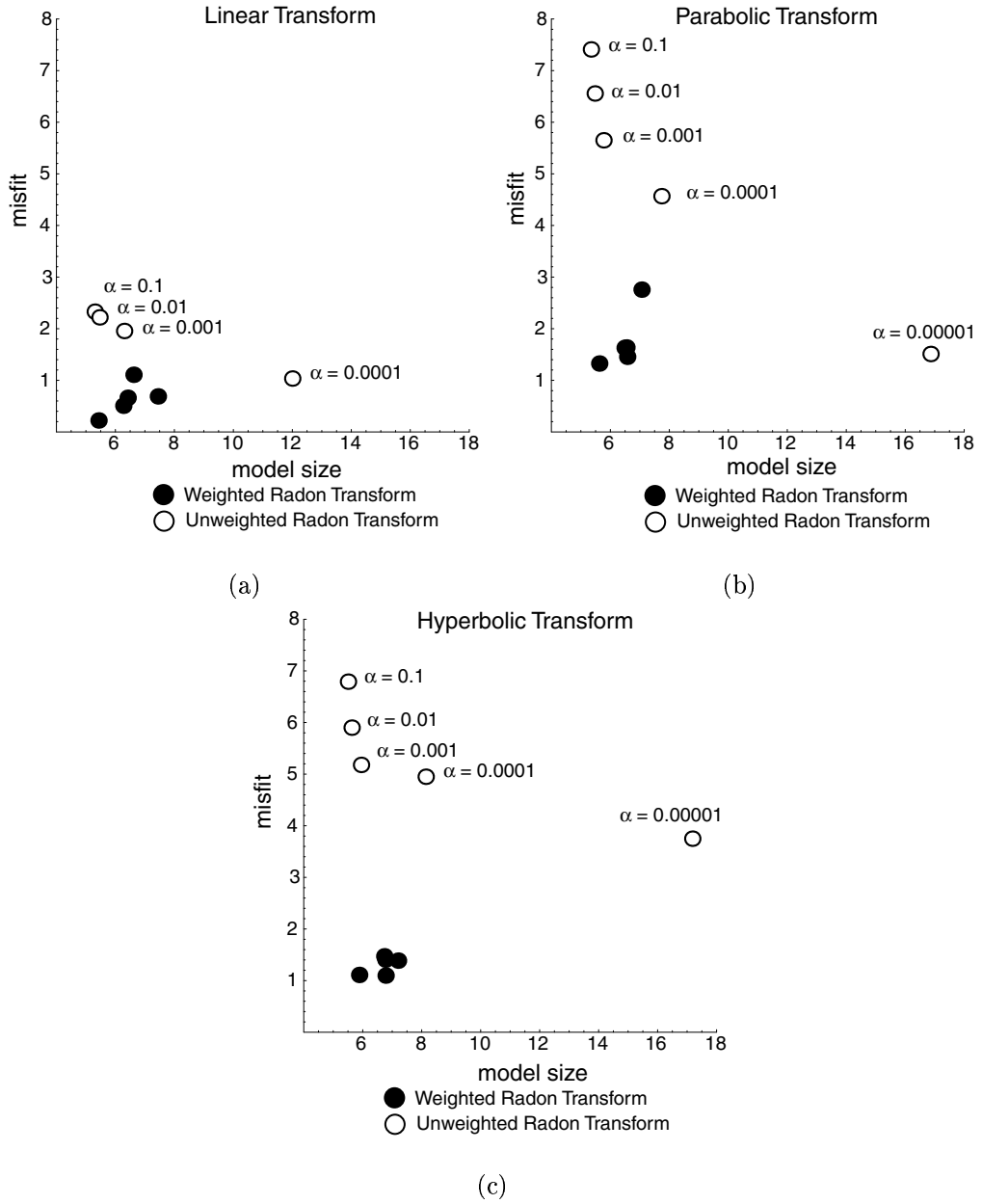

Figure 3.3: L_2-norm curves resulting from the filtering process depicted in Figures 3.1 and 3.1 for **(a)** linear, **(b)** parabolic, and **(c)** hyperbolic transforms.

3.4 Random noise

A similar model and filtering process, as depicted in Figures 3.1 and 3.2, was chosen to assess the effect of introducing random noise to the synthetic data. The weighted and unweighted solution to the parabolic Radon transform were used to suppress the hyperbolic events from

the synthetic NMO corrected data in the presence of 30% random noise. The results of this test, shown on Figure 3.4(a), are strikingly similar to those performed on the noise free synthetic data depicted in Figure 3.3(b). Based on this result, an α value of 0.0001 was chosen and the filtering process was systematically repeated for models with 10%, 20%, 30%, 40%, and 50% additive random noise. The results of this "noise test," shown on Figure 3.4(b), suggest that the performance of filters operating on the weighted solution Radon transform is less sensitive to the signal-to-noise ratio than those operating on an unweighted solution to the transform.

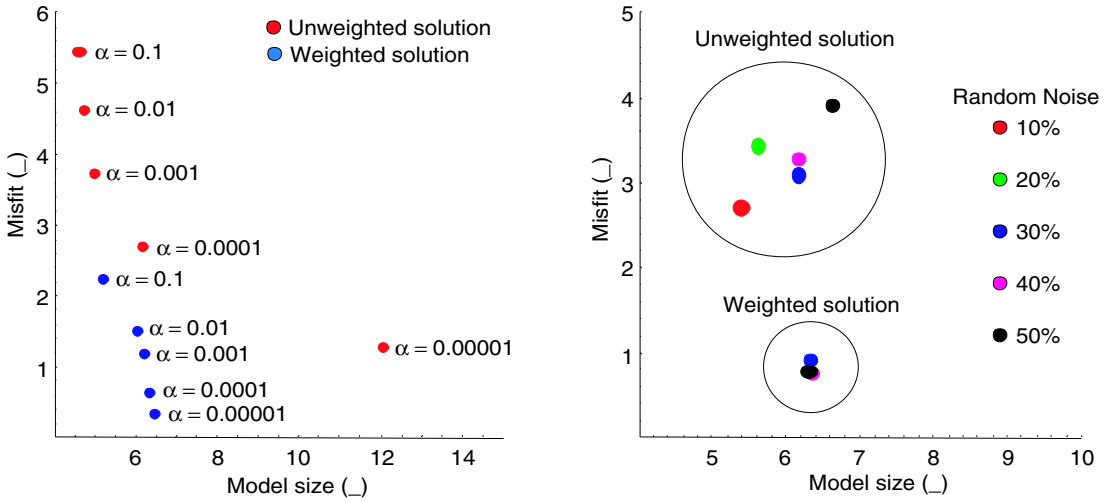

(a) (b)

Figure 3.4: L_2-norm curves showing the filtering results of using the weighted and unweighted solutions to the parabolic Radon transform **(a)** in the presence of 30% random noise with varying prewhitening factors and **(b)** with $\alpha = 0.0001$ and varying degrees of random noise.

3.5 Amplitude preservation

Historically, the main disadvantage of Radon filtering multiples is the reduction of reflector amplitudes on near and far offsets (Kabir and Marfurt, 1999). This phenomenon occurs when portions of the near and far offset artifacts, belonging to the Radon representation

of the reflectors in the transform domain, are truncated when the filter is designed. These artifacts, also reported by Kabir and Marfurt (1999), consist of the moveout spanning near offset artifact and the traveltime spanning far offset artifact observed on Figure 3.5(a). When the filters are designed to remove the events that map to negative and zero moveouts, portions of these artifacts associated with the primary reflections are left behind on the positive moveout side of the transformed domain. The multiples and portions of the near- and far-offset primary reflections are modeled upon inverse transformation and subtracted from the input CMP gather thus removing the multiples and needlessly reducing the near- and far-offset reflector amplitudes. However, when the weighted solution is used, the events are more localized in the Radon domain causing the near and far offset artifacts to be reduced (as shown on Figure 3.5(b)).

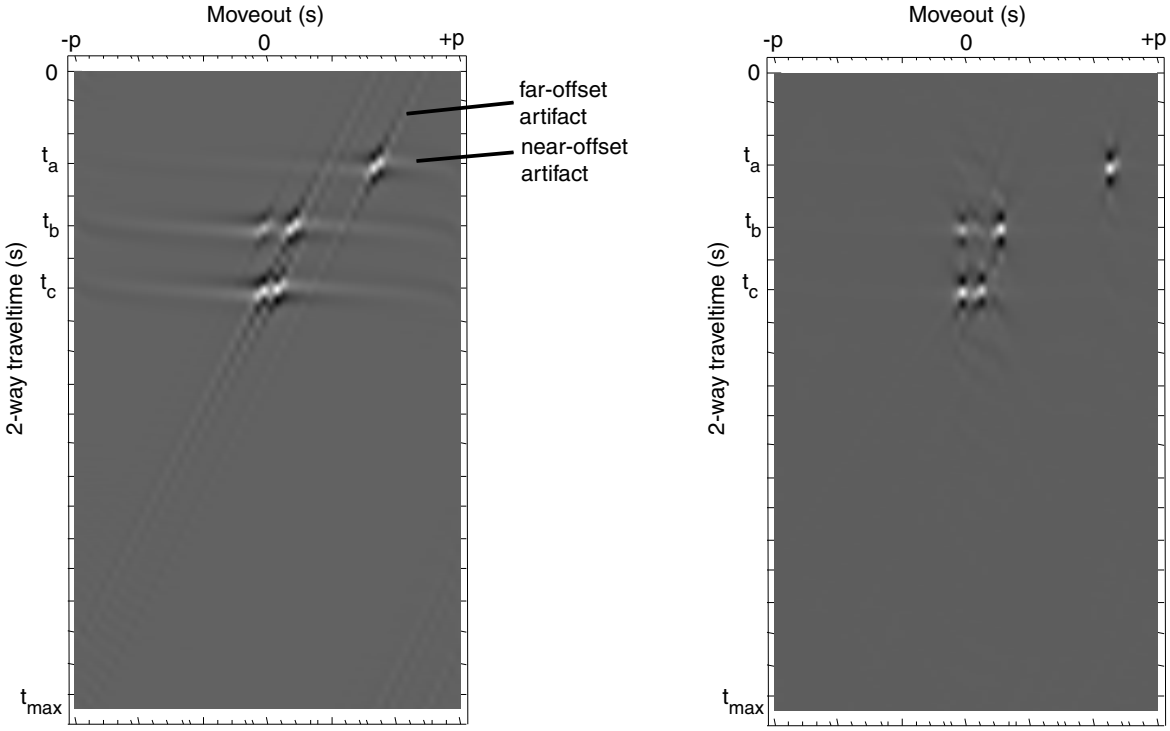

Figure 3.5: Showing the near- and far-offset artifacts **(a)** present in the unweighted Radon domain and **(b)** not present in the weighted Radon domain.

To observe the treatment of reflector amplitudes after Radon filtering multiples consider the synthetic NMO corrected CMP gather depicted in Figure 3.6. The weighted and unweighted solutions to the linear, parabolic and hyperbolic Radon transform were used to filter the synthesized water bottom multiples (shown as events exhibiting residual moveout). For this exercise, the reflector at 1.1 seconds (two-way traveltime) is treated as the target horizon. AVO plots along this reflector are shown before (blue) and after (red) filtering the multiples on Figure 3.7.

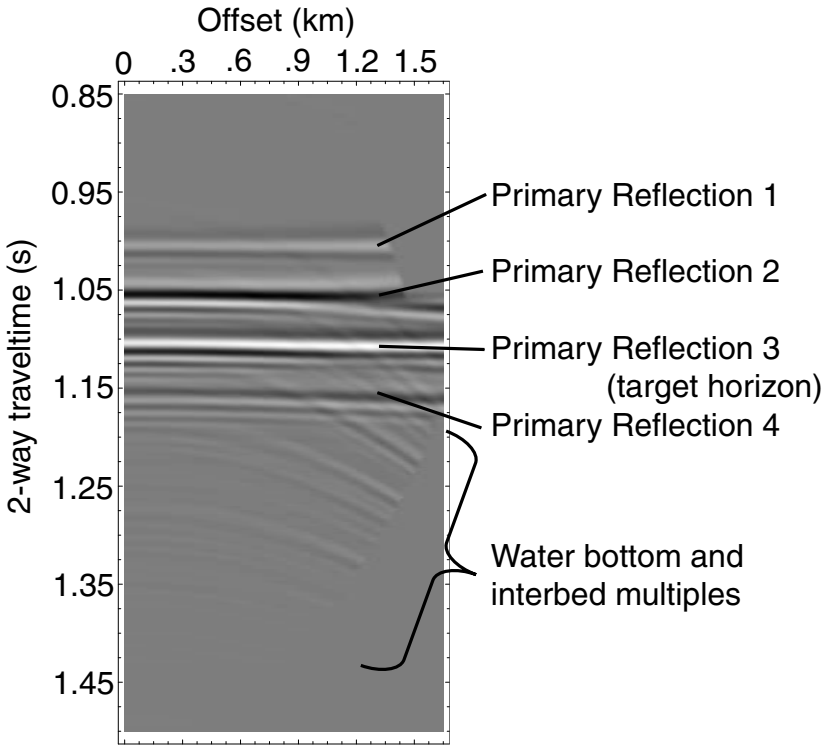

Figure 3.6: Portion of an NMO corrected synthetic CMP gather exhibiting the additive contamination of water bottom multiples on reflections.

As depicted on these AVO plots, the various Radon filters were able to remove much of the small-scale undulations caused by the additive contamination of the water bottom multiples. The filters resulting from the unweighted solutions, Figures 3.7(a), 3.7(c), and 3.7(e), caused a significant amplitude reduction at near and far offsets due to the aforementioned truncation

effect; whereas this effect was not present when the various weighted solutions, Figures 3.7(b), 3.7(d), and 3.7(f), were used to suppress the multiples. This suggests a better preservation of reflector amplitudes is achieved when the weighted solutions to the Radon transform are used to suppress multiple reflections.

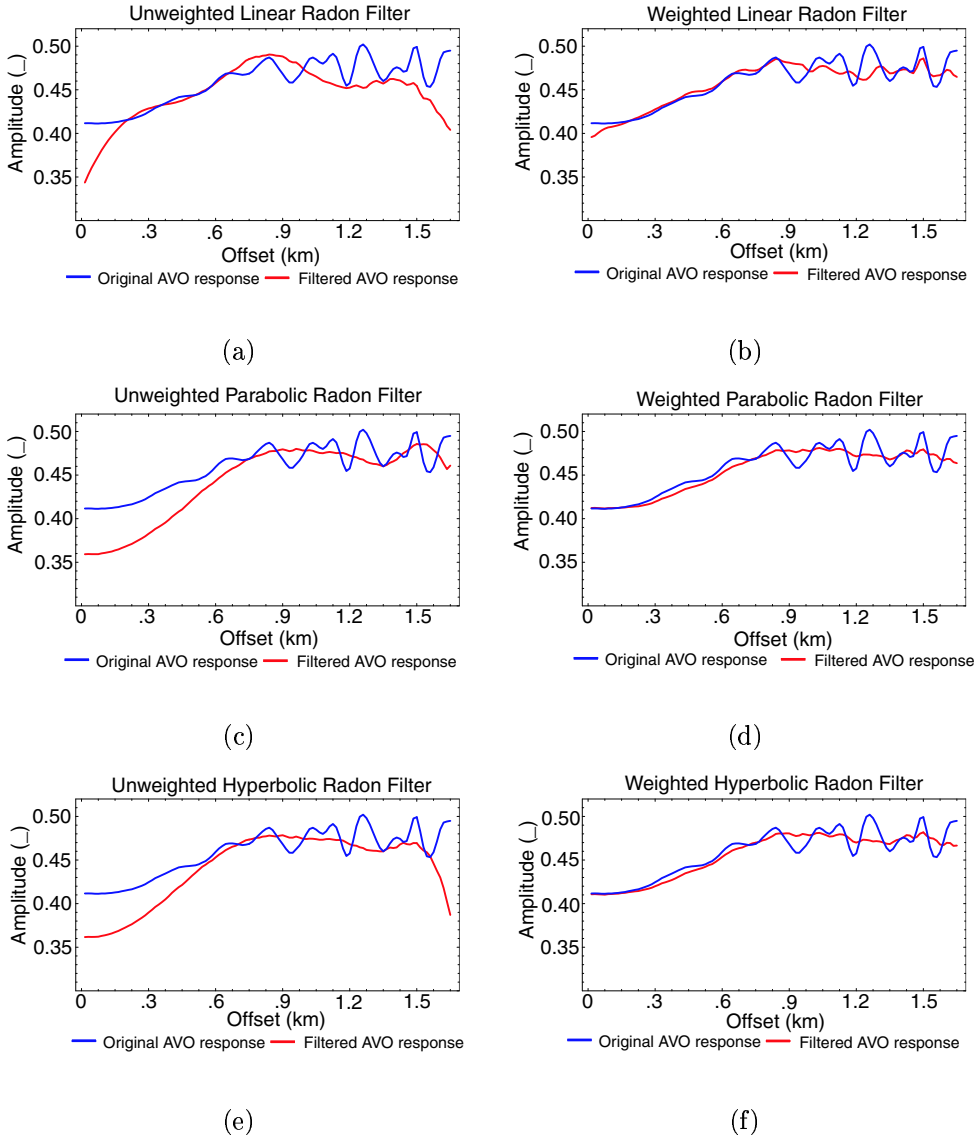

Figure 3.7: AVO plots along the reflector at 1.1 seconds (Figure 3.6) before and after Radon filtering the multiples with the **(a)** unweighted and **(b)** weighted linear transform, the **(c)** unweighted and **(d)** weighted parabolic transform, and the **(e)** unweighted and **(f)** weighted hyperbolic transform.

3.6 Conclusion

The motivation for this study was to assess the degree of reflector amplitude preservation after filtering long period multiple reflections with the Radon transform. The results agree with previous works (Kabir and Marfurt, 1999) in that the unweighted solution to the Radon transform reduces the near and far offset amplitudes due to a truncation artifact in the transform domain. However, the focusing aspect of the weighted solution localizes the Radon representation of the reflections, thus minimizing this truncation effect and preserving the near and far offset amplitudes. These synthetic experiments also suggest that the performance of filters operating on the weighted solution Radon transform is less sensitive to the signal-to-noise ratio than those operating on an unweighted solution to the transform.

In addition, the question of choosing a prewhitening factor, common in this inversion, is often experimental or even arbitrary when applied to field data. A suitable factor appears to play an important role in minimizing the data misfit and model size for the unweighted solutions, but is nearly irrelevant for the weighted solutions when applied to synthesized seismic data.

Chapter 4

Stacking seismic data without velocity analysis

4.1 Introduction

A typical seismic data processing flow contains some form of velocity analysis and normal moveout (NMO) correction prior to stacking common midpoint (CMP) gathers. The NMO correction renders the hyperbolic trajectory of reflections on CMP gathers nearly horizontal with respect to offset and at a depth coincident with the zero offset two-way traveltime. The traces within these corrected CMP gathers are then summed to produce a stacked seismic trace.

Similarly, in principle, the Radon transform has the ability to sum events exhibiting a hyperbolic trajectory in the space-time domain to a single event in the transformed domain. This single event is mapped to the intercept and moveout. As a result of this, Radon filtering has been a resounding success in suppressing multiple reflections from NMO corrected seismic data (Foster and Mosher, 1992; Trad et al., 2003). Due to the localization and position of these mapped reflection hyperbolas in the transformed domain, a stacked seismic trace can

also be produced by summing over moveout.

Because velocity analysis is often deemed "expensive" due to the required manual and interpretative selection of primary events and velocities, the purpose of this study is to develop a means to generate a stacked seismic section unaided by a velocity model. I propose to use the Radon transforms to generate a stacked section from CMP data without performing velocity analysis priorly. The Radon stack might be slightly noisier because events other than primary ones could get stacked in. On the other hand, NMO stretch is prevented and hence, no NMO stretch mute is necessary, which allows stacking of more samples.

4.2 Stacking processes

To illustrate and test the validity of using the weighted Radon transform, described in Appendix A, to generate a stacked seismic trace, consider the synthetic CMP gather depicted in Figure 4.1(a). Here the model consists of four primary reflections at 0.8, 0.875, 1.075, and 1.125 seconds (two-way traveltime). As can be seen on Figure 4.1(b), these reflections focus in the hyperbolic Radon domain into four localized events at their respective moveout and intercept times. For comparison the CMP gather has been corrected for normal moveout with a perfect velocity model and an allowable stretch mute of 1.3. The resulting gather is depicted in Figure 4.1(c). A stacked seismic trace is generated by summing the Radon representation of the traces (Figure 4.1(b)) over moveout and summing the NMO corrected traces (Figure 4.1(c)) over offset. These stacked seismic traces are shown on Figures 4.1(d) and 4.1(e) and compared to the zero offset trace extracted from Figure 4.1(a).

The suitability of these stacking techniques is quantified by the normalized crosscorrelation function Equation 2.1. For these two cases the actual outcome $S(t)$ is the Radon and NMO stacked traces shown on Figures 4.1(d) and 4.1(e), and the desired outcome $R(t)$ is the zero offset trace also shown on these figures.

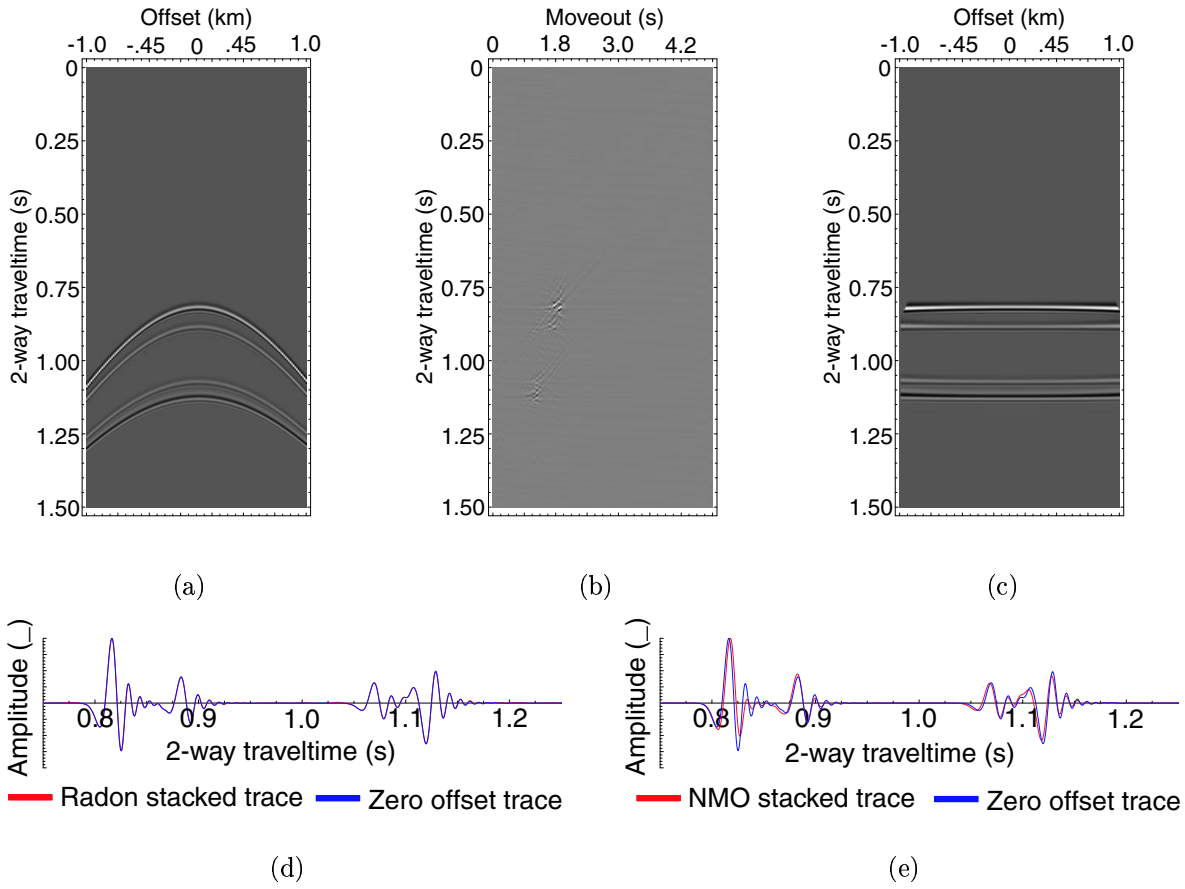

Figure 4.1: Depicts **(a)** synthetic CMP gather; **(b)** weighted hyperbolic Radon transform of **(a)**; **(c)** after correcting **(a)** for normal moveout; **(d)** Radon stacked trace; and **(e)** NMO stacked trace.

For this synthetic example, when the CMP gather was stacked using the Radon transform a 99.8% match was achieved, whereas an 88.8% crosscorrelation between the NMO stacked and zero offset traces was attained. Even though the CMP gather was corrected for normal moveout with a perfect velocity model, distortions were introduced by NMO stretching. Ideally any sample that is stretched after correcting for normal moveout should be set to zero, however in practice, this is not realistic, and hence, a NMO stretch mute of 1.3 was applied.

4.3 Application to field data

The above stacking techniques were also applied to CMP gathers collected offshore Nigeria. All gathers were amplitude corrected. Predictive deconvolution was applied twice to remove water-bottom reverberations and short-period multiples. The seismic section, shown on Figure 4.2(a), was produced by velocity analysis followed by NMO correction and subsequent stacking. The Radon stacked seismic section, shown on Figure 4.2(b), was produced by weighted hyperbolic Radon transform of each CMP gather, which were then summed over positive moveouts and followed by a poststack automatic gain control (AGC) to balance the stacked seismic traces.

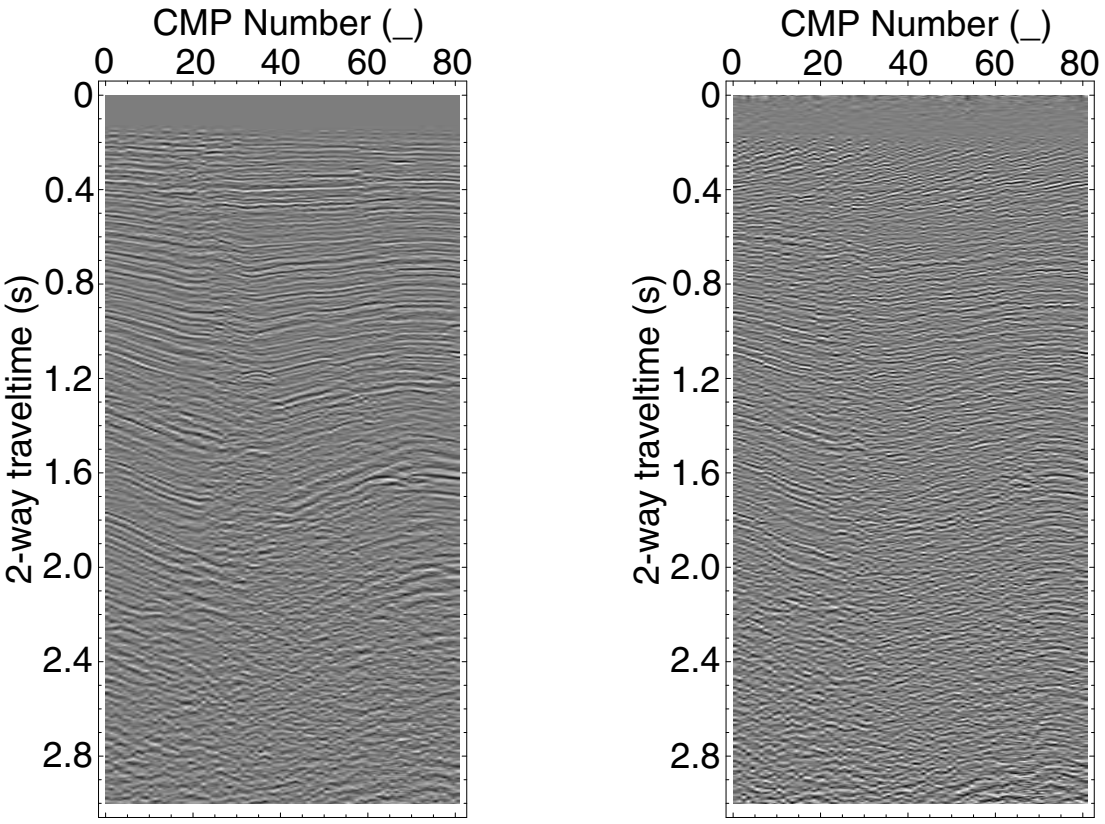

(a) (b)

Figure 4.2: Depicting the results of stacking offshore field data **(a)** after NMO correction; **(b)** with the weighted hyperbolic Radon transform.

The non-geologic features present in the Radon stacked section, particularly above 0.4 seconds, are not found on the NMO stacked section. The shallow artifacts present in the Radon stacked section, shown on Figure 4.2(b), are attributed to the lack of offset signal samples at shallow depths in the CMP gathers. Consider the CMP gather shown in Figure 4.3(a). Because there are fewer recorded samples at shallow depths in the offset direction, many hyperbolas with different moveouts can model the reflections. These shallow reflections are then represented as the moveout spanning events in the Radon domain shown on Figure 4.3(b). Because these moveout spanning events do not necessarily occur at a constant two-way traveltime they distort the appearance of the reflection upon stacking.

However, the NMO and Radon stacked sections below 0.4 seconds on Figures 4.2(a) and 4.2(b) are strikingly similar and yield comparable stratigraphic interpretations. This agreement between the two stacked seismic sections is confirmed on the enlarged subsets shown on Figures 4.4(a) and 4.4(b).

4.4 Conclusion

We extended the use of the weighted hyperbolic Radon transform to generate stacked seismic sections from CMP gathers. This technique has the advantage over the traditional stacking of NMO corrected CMP gathers because it does not rely on a velocity model. Circumventing the need for velocity analysis to produce a stacked seismic section or volume reduces the man hours required to process surface recorded seismic data. The results of the synthetic example suggest the theory is sound and has promise. When the technique was applied to field data from offshore Nigeria, the resulting Radon stack image was comparable to the NMO stack barring some artifacts at shallow depths. Applications include rapid processing for quality control purposes, initial examination of data, or other applications where automated and largely unsupervised seismic data processing is needed.

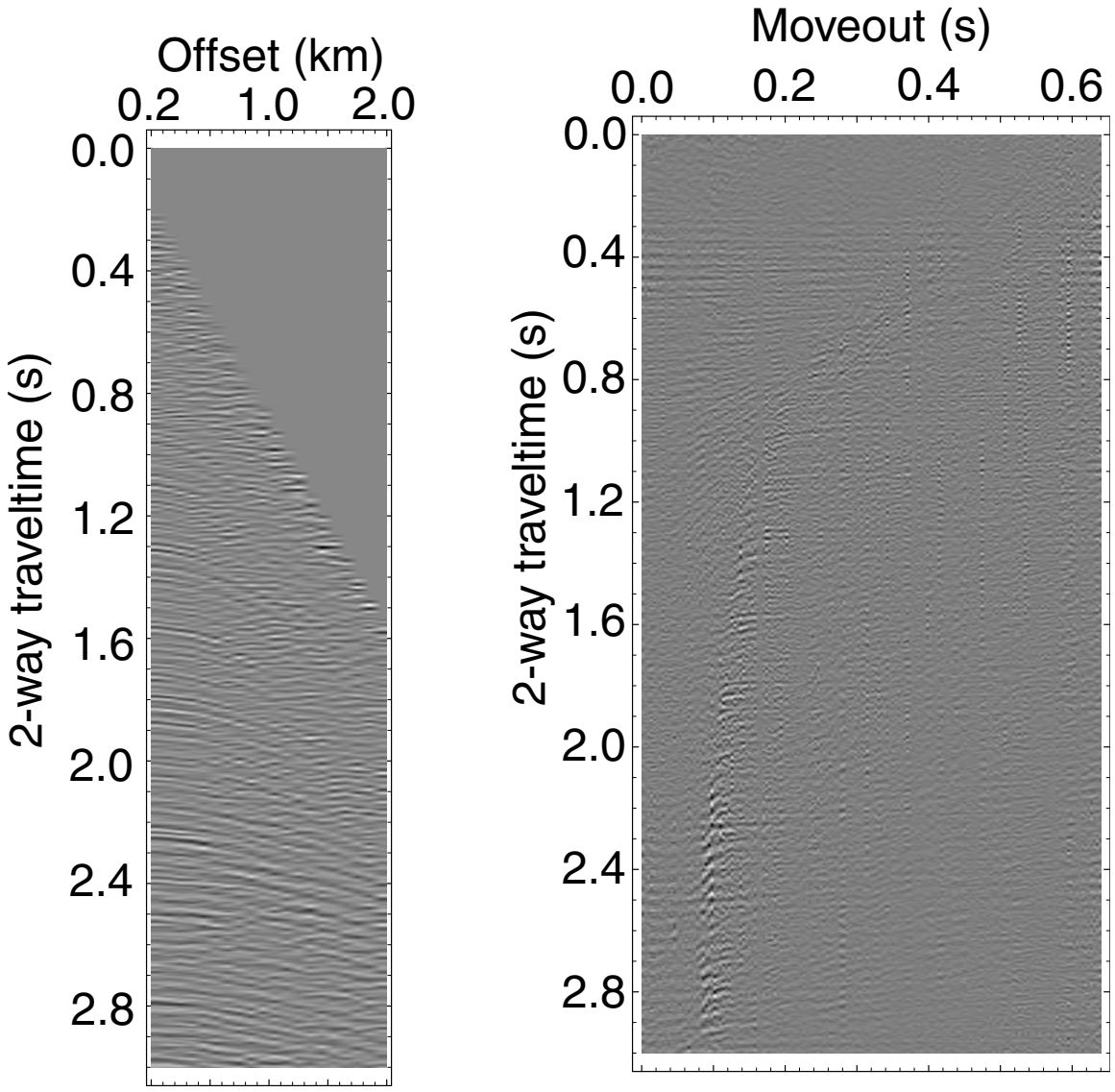

(a) (b)

Figure 4.3: Depicting **(a)** common midpoint gather from offshore Nigeria and **(b)** the weighted hyperbolic Radon transform of **(a)**.

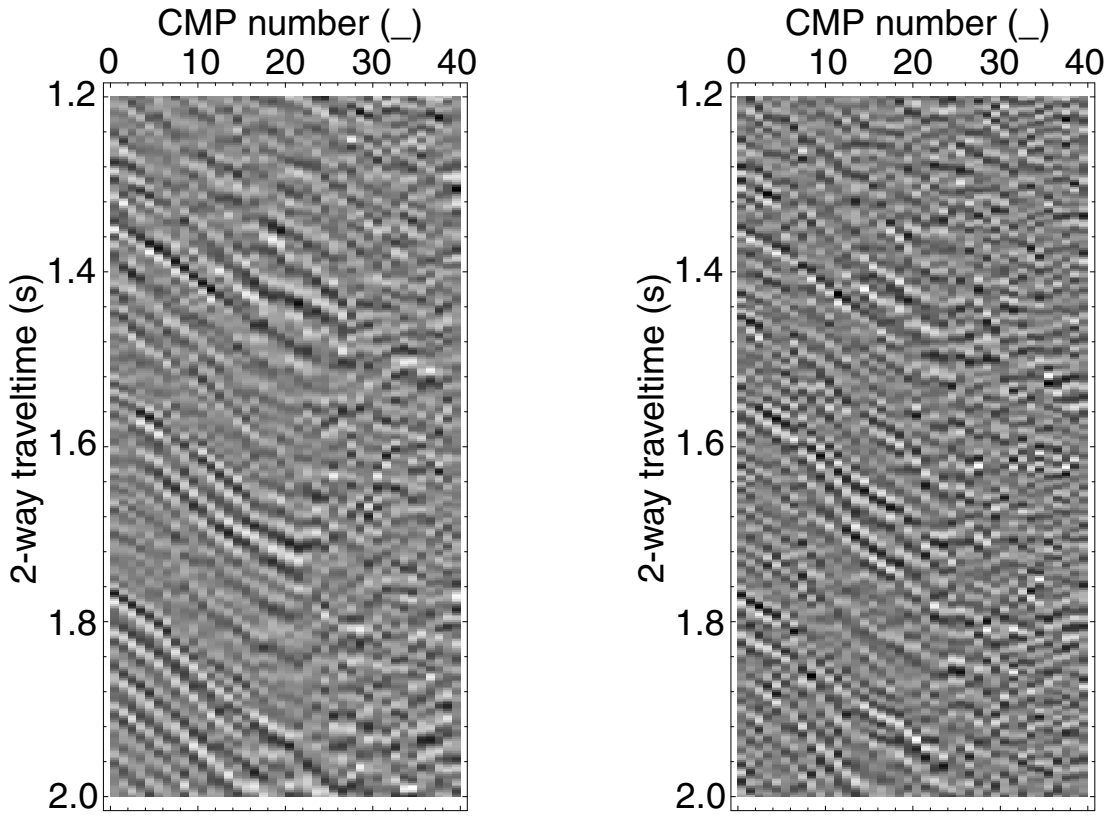

(a) (b)

Figure 4.4: Depicting **(a)** a subset of Figure 4.2(a); and **(b)** a subset of Figure 4.2(b).

Chapter 5

Stratigraphic filtering

5.1 Introduction

Stratigraphic filtering is a phenomenon that has been reported by numerous authors (e.g., O'Doherty and Anstey, 1971; Banik et al., 1985a,b). In general, this phenomenon is observed in reflected and transmitted wavefields as a signal propagates through a material exhibiting thin periodic lamina or layers. In this context, thin refers to the thickness of the individual layers when deterministically unresolvable by a reflection (i.e. $< \frac{1}{4}$ wavelength, λ). When the direction of propagation is perpendicular to the layering, the material acts as a frequency filter that alters the shape of the reflected and transmitted signals. The shaping of these signals, caused by the filter, is due to the amplification or attenuation of certain sinusoidal components of the incident signal. Deng (1994) reported that for a normal incident seismic signal propagating through thin periodic layers, the interference of short-period multiples attenuates the high frequencies of the transmitted signal. Signals propagating obliquely to layering may experience an additional loss of high frequencies through evanescent filtering, a phenomenon caused by the preferential tunneling of lower frequencies within higher velocity thin layers (Deng, 1994).

The purpose of this study is to propose an alternative explanation for the cause of stratigraphic filtering and examine which information can be derived from this phenomenon to provide an insight towards thin layer detection. Both an analytical solution and numerical modeling of zero-offset acoustic wave propagation were used to investigate its cause. The analytical solution was facilitated by an acoustic layer stack scheme (Imhof, 2003), which allows direct calculation of the reflection and transmission coefficients. The numerical modeling technique is based on a space-time finite-difference approximation to the scalar wave equation (Jensen et al., 1994), which provides a means of calculating the reflected and transmitted wavefields. Wavefields and spectra were calculated for layer stacks of various layer thicknesses and periodicities.

Before discussing stratigraphic filtering, I outline a possible mathematical analogy, namely Bragg scattering or Bragg reflection from Sheng (1995), that can be used to describe the phenomenon of waves propagating in periodic media.

5.2 Bragg scattering

Bragg scattering is observed in the use of plane wave propagation along a linear, elastic, homogeneous, isotropic, and periodic lattice as depicted in the 1-D model of nodes shown in Figure 5.1.

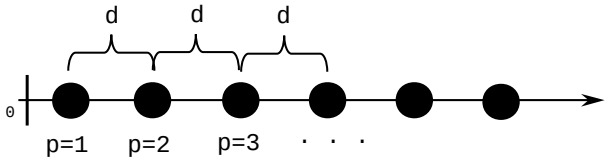

Figure 5.1: 1-D model of n nodes separated by a distance d where each node is characterized by the same acoustic velocity and identified by the integer p.

To illustrate this phenomenon, consider the following 1-D scalar wave equation

$$\frac{d^2U}{dt^2} = \frac{E}{\rho}\frac{d^2U}{dx^2}, \tag{5.1}$$

where E and ρ denote a constant Young's modulus and density on the lattice with node spacing d. The spatial derivative with respect to displacement U on the right hand side can be rewritten as a differencing equation of order two:

$$\frac{d^2U_p}{dt^2} = \frac{E}{\rho d^2}(U_{p+1} + U_{p-1} - 2U_p), \tag{5.2}$$

where p refers to the node index. Assuming harmonic plane wave displacements

$$U = Ae^{i(kpd-\omega t)} \tag{5.3}$$

where A denotes a constant amplitude, ω refers to angular frequency, k is wavenumber and distance $x = pd$, where $p = 1, 2, 3, \ldots$. We substitute (5.3) into (5.2), evaluate the temporal derivative, and utilize Euler's relationship $e^{i\alpha} = \cos\alpha + i\sin\alpha$ to obtain the dispersion relation

$$\omega(k) = \frac{2}{d}\sqrt{\frac{E}{\rho}}\sin\frac{kd}{2}. \tag{5.4}$$

Group velocity describes the speed with which energy propagates as a function of k. It is calculated by differentiating the dispersion relation (5.4) with respect to wavenumber:

$$v_G = \frac{d\omega(k)}{dk} = \sqrt{\frac{E}{\rho}}\cos\frac{kd}{2}. \tag{5.5}$$

This group velocity $v_G(k)$ exhibits two different behaviors. As can be seen from equation

(5.5), the case where $k > \pi/d$ results in a negative group velocity, which corresponds to ultimate dispersion where the signal is incapable of penetrating the lattice. For the case where $k < \pi/d$, the group velocity attains a positive value and the signal propagates along the lattice without distortion. At the threshold $k = \pi/d$, the group velocity is zero which corresponds to a standing wave (Sheng, 1995). This latter case is the Bragg scattering phenomenon. This effect dictates the high-frequency limit of wave propagation on a lattice, but the typical frequencies utilized in geophysical studies do not approach this limit. By using this Bragg scattering analogy and introducing 1-D periodic heterogeneity to the model, the stratigraphic filtering phenomenon may be explained.

5.3 Frequency filtering in periodic layerstacks

To explore the cause of stratigraphic filtering, consider the addition of a material periodicity to the 1-D model as shown in Figure 5.2.

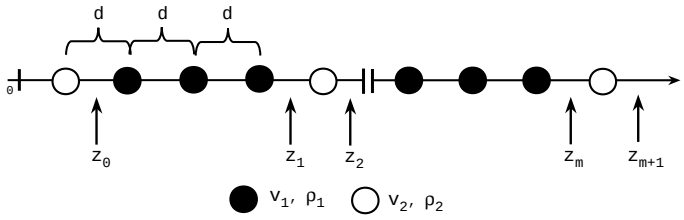

Figure 5.2: 1-D model of nodes separated by the distance d exhibiting a material periodicity introduced by systematic changes in acoustic velocity v. The locations z_i separate the different homogeneous zones within the lattice.

With the introduction of the material periodicity to the 1-D model, difficulties arise when attempting to achieve a solution similar to the mathematical Bragg scattering analogy. However, it can be described analytically by an acoustic layer stack scheme or numerically by a space-time finite difference approximation to the scalar wave equation.

Analytical solution

The layer stack technique allows for the direct calculation of the reflection $R(\omega)$ and transmission $T(\omega)$ spectra produced by a plane wave propagating through a stack of layers with equivalent geometry to the one shown in Figure 5.2. A propagator matrix $\mathbf{P}_\ell$

$$\mathbf{P}_\ell = \begin{bmatrix} e^{+i(z_{\ell+1}-z_\ell)k_{\ell+1}} & 0 \\ 0 & e^{-i(z_{\ell+1}-z_\ell)k_{\ell+1}} \end{bmatrix} \tag{5.6}$$

is used to extrapolate the waves from an interface ℓ at depth z_ℓ to interface $\ell+1$ at depth $z_{\ell+1}$ and vice versa. The vertical wavenumber $k_{\ell+1} = \sqrt{(\frac{\omega}{v_{\ell+1}})^2 - p^2}$, consists of the medium wavenumber $\frac{\omega}{v_{\ell+1}}$ and the horizontal wavenumber p. A transition matrix $\mathbf{V}_\ell$

$$\mathbf{V}_\ell = \frac{1}{2}\begin{bmatrix} 1+\xi_{(\ell+1)\ell} & 1-\xi_{(\ell+1)\ell} \\ 1-\xi_{(\ell+1)\ell} & 1+\xi_{(\ell+1)\ell} \end{bmatrix} \qquad \text{where} \qquad \xi_{ij} = \frac{\rho_i v_i}{\rho_j v_j} \tag{5.7}$$

based on the impedance ratios between adjacent layers governs the behavior of the plane waves propagating at the interface between layers ℓ and $\ell+1$. Thus, reflection $R(\omega)$ and transmission $T(\omega)$ coefficients for the entire layer stack can be directly calculated by coupling the propagator and transition matrices

$$\begin{bmatrix} 0 \\ T(\omega) \end{bmatrix} = \mathbf{V}_m \cdot \left\{ \prod_{\ell=0}^{m-1} \mathbf{P}_\ell \cdot \mathbf{V}_\ell \right\} \cdot \begin{bmatrix} R(\omega) \\ 1 \end{bmatrix}. \tag{5.8}$$

The accuracy and numerical stability of the matrix product equation (5.8) can be tested by considering the conservation of energy $|R(\omega)|^2 + \xi_{0n}T(\omega)|^2 = 1$ (Imhof, 2003).

As an example, the reflection and transmission coefficients were calculated for a layer stack consisting of alternating layers with thicknesses of 2 ft (0.61 m) and 34 ft (10.4 m) and velocities 6250 ft/s (1905 m/s) and 5000 ft/s (1524 m/s), respectively. For simplicity,

the density remained constant and was set to one. In this example, the layer stack exhibits a spatial periodicity of 36 ft which corresponds to a temporal periodicity on the order of 0.0142 s or a material frequency of 70 Hz. This material frequency is defined by the inverse Wyllie time average

$$f_{\text{material}} = \left(\sum_{n=1}^{N} \frac{h_n}{v_n} \right)^{-1}, \tag{5.9}$$

modified from Wyllie et al. (1957), over a single spatial period of the layer stack. In this expression, h_n and v_n denote the thickness and velocity of the n^{th} layer.

This material frequency establishes a fundamental frequency or resonance which corresponds to the first major peak on the reflected energy spectrum, $|R(\omega)|^2$, shown in Figure 5.3(a) and the first major trough on the transmitted energy spectrum, $|T(\omega)|^2$, shown in Figure 5.3(b). Note the frequencies associated with the integral multiples of the fundamental frequency (harmonic series) correspond to major troughs and peaks on the transmitted and reflected energy spectra. This indicates that the sinusoidal components of the incident signal corresponding to the spatial periodicity of the material are preferentially reflected and hindered from propagating through the material.

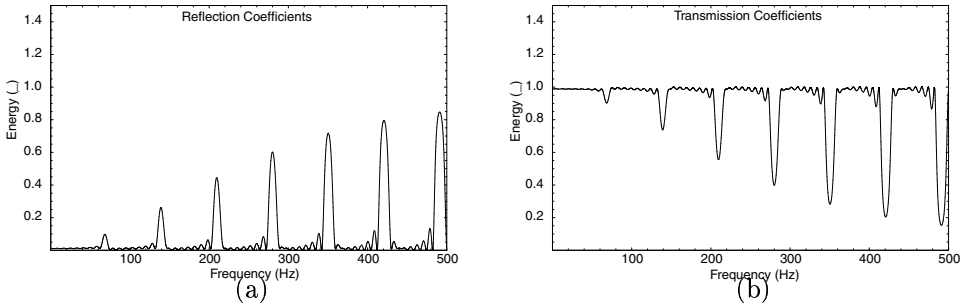

Figure 5.3: The energy spectra for the **(a)** reflection and **(b)** transmission coefficients.

Numerical solution

This preferential reflection anomaly from the periodic layer stack can be confirmed with a numerical solution computed with a space-time finite difference approximation to the scalar wave equation, outlined in Equations (B.1 - B.4) in Appendix B. Figure 5.4(b) depicts the reflected wavefield response to propagating a Ricker wavelet with a 60 Hz center frequency through the 1-D velocity model shown in Figure 5.4(a). For comparison purposes, this velocity model is shown as a function of two-way traveltime and is equivalent to the model previously shown in Figure 5.2.

As expected, the reflection from the top and bottom of the initial layer can be identified by wavelets with zero and 180° phases shown in red and green, which correspond to the skewed Gaussian energy spectra depicted in Figures 5.5(a) and 5.5(b). The reflected wavefield from the periodic layers (shown in blue) rendered little deterministic resolution of the periodic thin layers. Because the thickness of the thin layers used to establish the periodic heterogeneity was less than $\frac{\lambda}{4}$, their interfaces were not resolvable by a reflected Ricker wavelet. However, the response of propagating the wavelet through the layer stack produced a sinusoidal reflection. This sinusoidal reflection is represented as a narrow peak of elevated energy as shown on Figure 5.5(c). This coda-like reflection is followed by another zero phase wavelet including a small amplitude sinusoidal trail (shown in black) reflected from the base of the layer stack. This basal reflection is characterized by a skewed Gaussian energy spectrum similar to those depicted in Figures 5.5(a) and 5.5(b), however, containing a narrow trough of reduced energy as shown on Figure 5.5(d).

As in the previous discussion, the energy peak located at 70 Hz in Figure 5.5(c) coincides with the inverse Wyllie time average equation (5.9) over one spatial period of the material. This observation not only confirms the preferential reflection of the sinusoidal components of the incident signal that corresponds to the periodicity of the material, but also suggests that the inverse Wyllie time average is a suitable estimator of this material frequency. Note

the energy scale on Figure 5.5(c) is approximately 33 times larger than that of the other energy spectra shown in Figure 5.5.

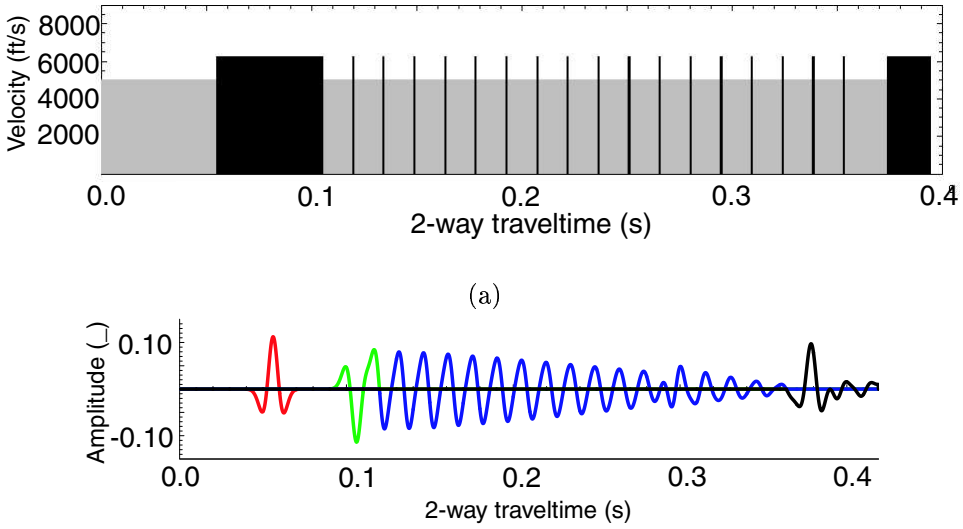

(a)

(b)

Figure 5.4: 1-D velocity model containing a periodic layer stack **(a)** and the reflected wavefield **(b)** showing the windows used to calculate the energy spectra shown in Figure 5.5.

Again, the frequencies associated with elevated reflected energy coincide with reduced transmitted energy as depicted on Figure 5.6. The accuracy and numerical stability of the finite differencing scheme can be tested by considering the conservation of energy, $|R(\omega)|^2 + \xi_{0n}|T(\omega)|^2 = |I(\omega)|^2$.

5.4 Discussion

The narrow band or bands of reduced energy observed on Figures 5.3(b) and 5.5(d), and on the transmitted energy spectrum shown on Figure 5.6 are the result of propagation through the layer stack. The stratigraphic filtering or any frequency filtering process is described as a time domain convolution of an input signal with a filter function which corresponds to a multiplication of their spectra in the frequency domain. Therefore, the narrow band of

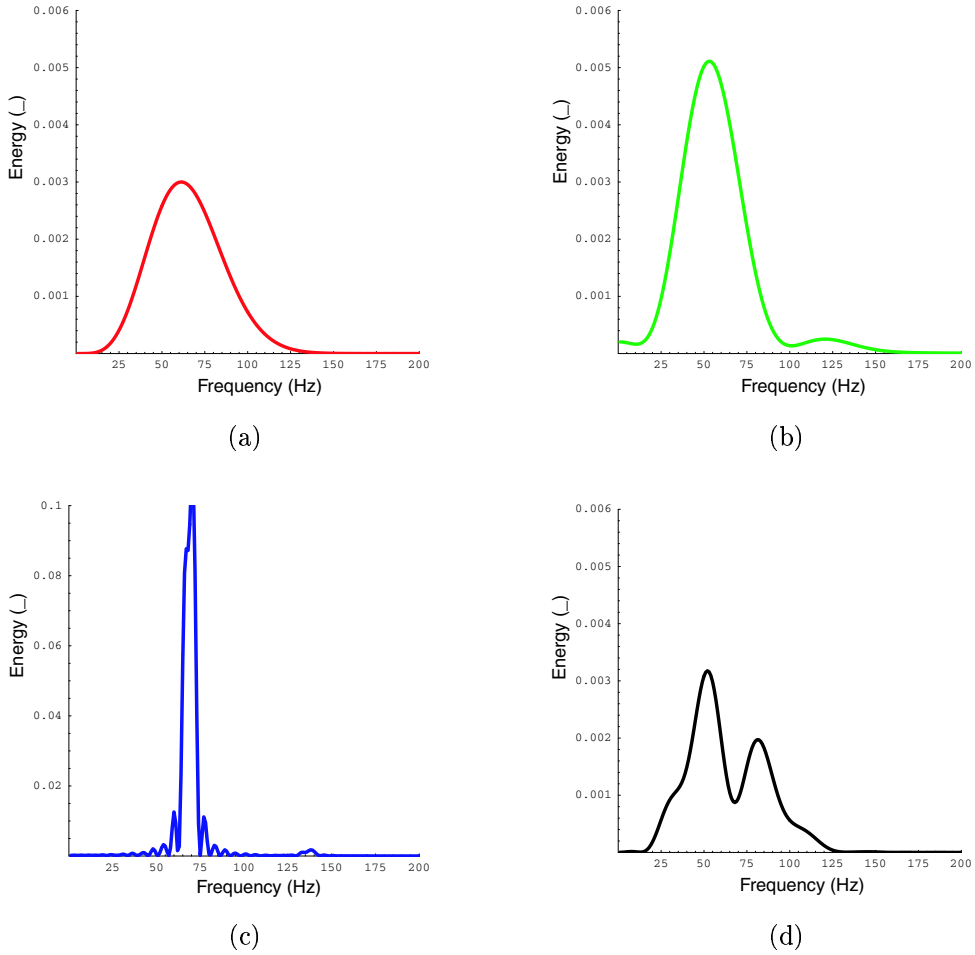

Figure 5.5: The reflected energy spectra resulting from **(a)** the top of the initial layer, **(b)** base of the initial layer, **(c)** the layer stack, and **(d)** base of the layer stack.

reduced energy observed on Figure 5.5(d) and the corresponding reflection from the base of the layer stack, shown in black on Figure 5.4(b), can be explained by the Fourier-time pairs shown in Figure 5.7.

The resultant Fourier amplitude spectrum produced by the multiplication of the incident and filter spectra shown in Figure 5.7 resembles that of the spectrum depicted in Figure 5.5(d). Similarly, the waveform produced by the convolution of the incident signal and the filter function resembles the reflected wavefield within the window used to calculate the energy spectrum shown in Figure 5.5(d).

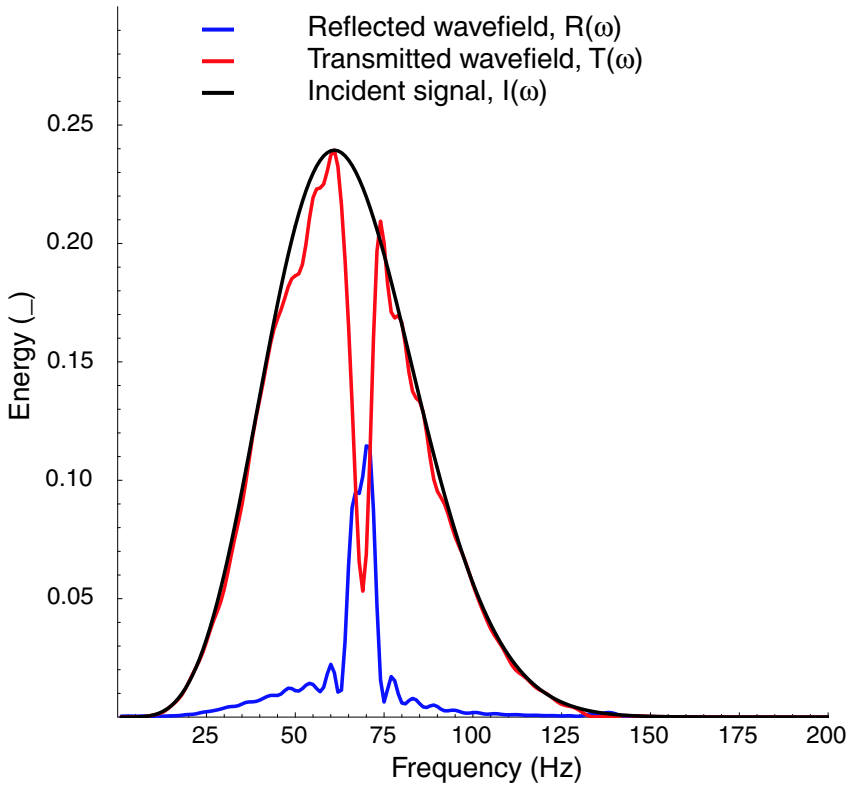

Figure 5.6: Energy spectra for the entire reflected and transmitted wavefields and the incident signal.

These frequency dependent amplitude reductions, also reported by Deng (1994), can only be observed by including the 70 Hz sinusoidal part of the signal within the window for calculating the energy spectrum. The filtering process affects the shape of the transmitted and reflected wavelets. As shown in Figure 5.7, the sinuous tail of the waveform corresponds to a reduction or removal of a single frequency or a band of Fourier coefficients from the incident signal. To restore the shape of the incident signal, the reduced or removed frequencies need to be boosted or added back to the spectrum. Hence the removal of frequencies from a signal has the effect of introducing those frequencies with opposite polarity in the time domain wave form, thus the sinuous trail predominately consists of 70 Hz energy as depicted on Figure

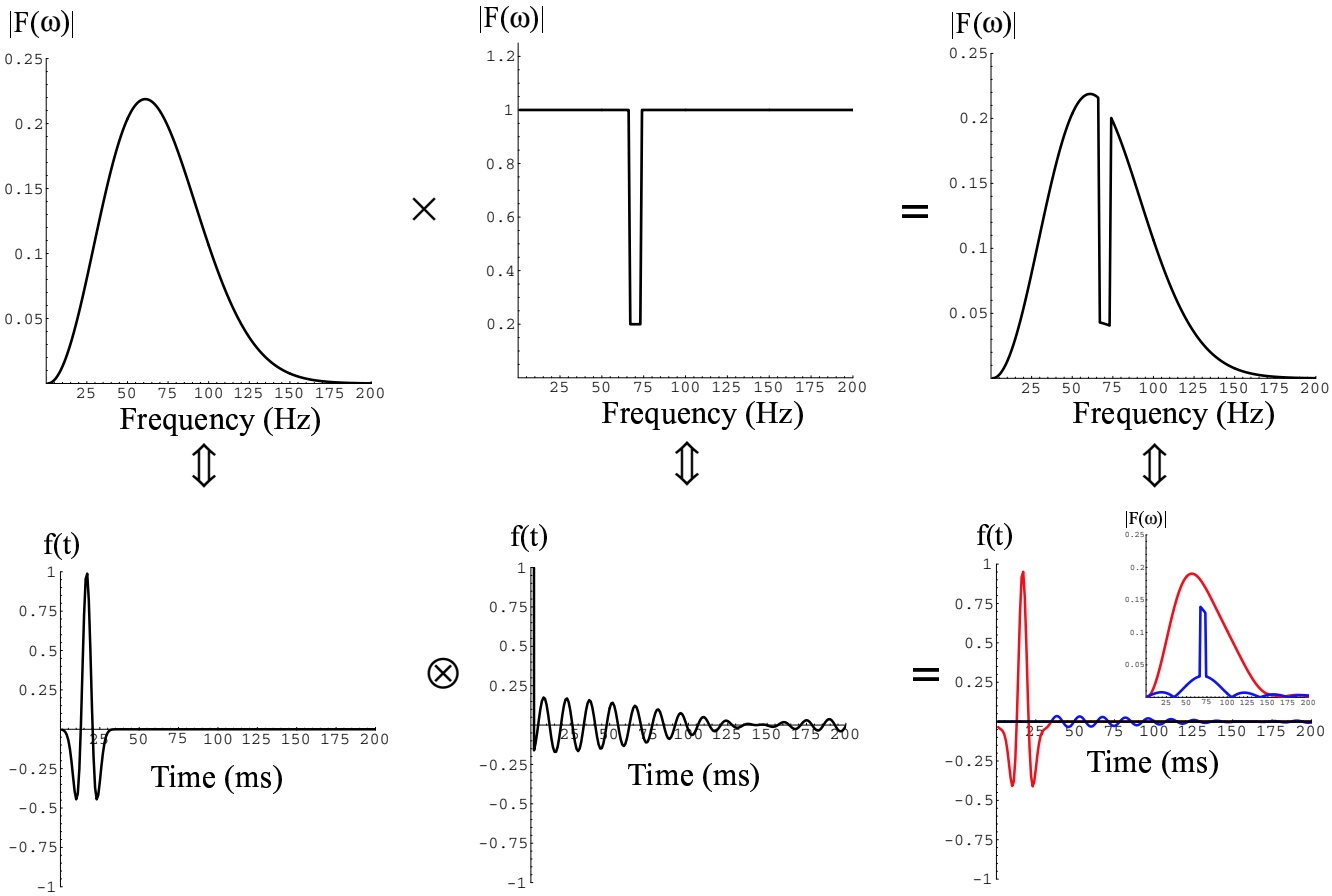

Figure 5.7: Fourier transform pairs depicting the filtering process. Note the 70 Hz trail observed in the resultant time-domain waveform due to the 70 Hz notch filter.

5.7. Omitting the sinuous trail from the window used to calculate the energy spectrum has the same effect as removing the notch filter as shown in Figure 5.7.

The stratigraphic filtering phenomenon can be explored further by adjusting the thicknesses of the layers contained in the stack while preserving the natural resonance frequency of the material. The models were chosen such that the material frequency of the layer stack remained constant at 70 Hz. However, the thickness, h_1, of the layers characterized by a velocity $v_1 = 6250$ ft/s was increased from 2 to 46 ft (14 m), while the thickness, h_2, of the layers characterized by a velocity $v_2 = 5000$ ft/s was decreased accordingly to comply

with equation (5.9). As can be seen on Figure 5.8, the frequency corresponding to the mean energy, calculated by Equation (B.8) in Appendix B, remained relatively constant, which suggests that the inverse Wyllie time average over one spatial period of the material is a suitable estimator for the resonance frequency of this material.

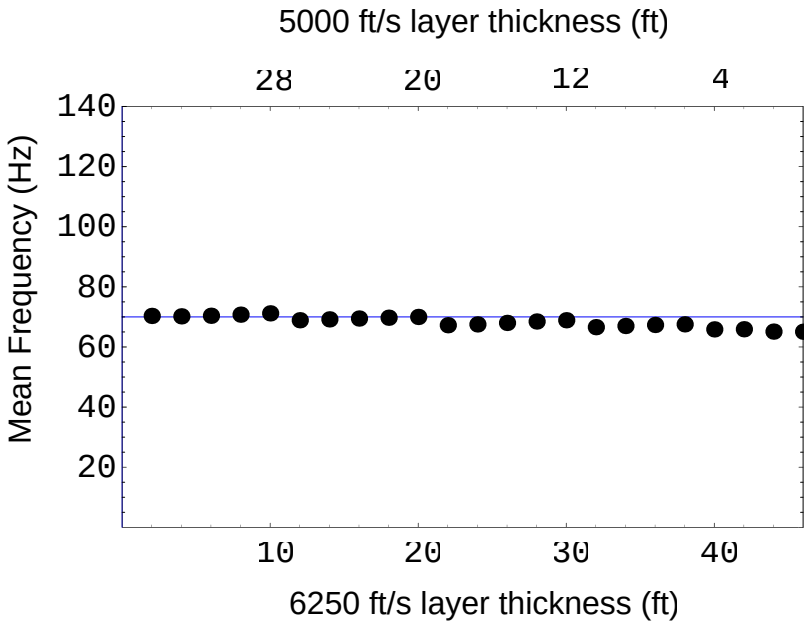

Figure 5.8: Cross-plot showing mean frequency as a function of varying layer thicknesses calculated from their Fourier derived energy spectra.

Figure 5.9 depicts the bandwidth, calculated by Equation (B.9) in Appendix B, of the energy spectra verses layer thickness for the previously described suite of models. By increasing one layer thickness and decreasing the other to maintain the same material frequency, the bandwidth of the energy spectra increases to a maxima. This maximum occurs when the traveltime through the two individual layers is approximately the same. For this example, the threshold occurs when the thickness of the 6250 ft/s layer is 22 ft (6.7 m) and the 5000 ft/s layer is 18 ft (5.5 m) thick. Beyond this threshold, the bandwidth decreases again.

This trend can be explained by considering the two cases described on Figure 5.10. As a convention, the layers characterized by a lesser travel time establish the periodicity of the

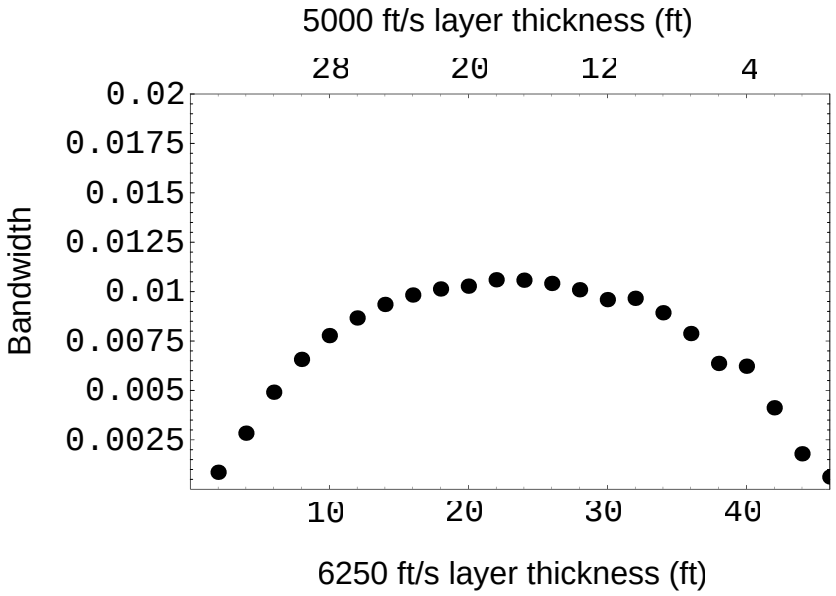

Figure 5.9: Cross-plot showing varying layer thicknesses as a function of bandwidth calculated from their Fourier derived energy spectra.

binary material. When these layers are thinner, as depicted on Figure 5.10(a), fewer plane waves resonate within the material, which fosters a narrow band of reflected energy. As the traveltime through the thinner layers approaches that of the alternating layers, the greatest number of plane waves resonate as reflections as shown in Figure 5.10(b); hence the broad reflected energy spectrum.

5.5 Conclusion

Effects of stratigraphic filtering were explored by adding a material periodicity to the 1-D model. The results of the analytical solution and numerical modeling indicate that the sinusoidal components of the incident signal resonating with the periodicity of the material are preferentially reflected as opposed to attenuated by the interference of short period multiples. These preferentially reflected sinusoids are contained in a relatively narrow frequency band. This band of elevated energy coincide with the inverse Wyllie time average of the material

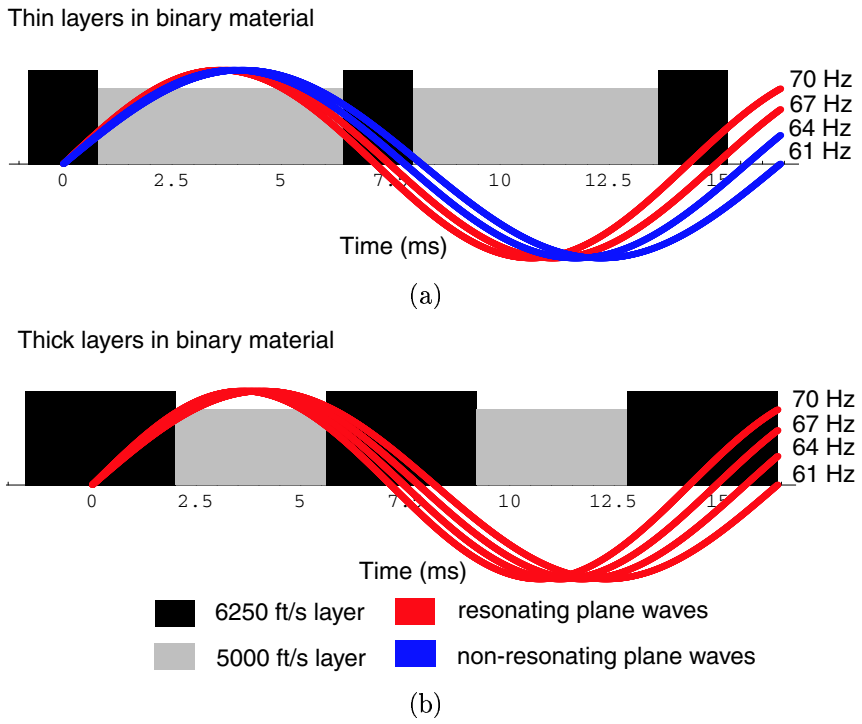

Figure 5.10: Examples of **(a)** thin and **(b)** thick layers establishing a 70 Hz binary material.

over a single spatial period. This frequency corresponds to the traveltime distance between the layers used to establish the periodicity. The bandwidth of the peaks is proportional to the traveltime thickness of the layers used to establish the periodicity of the material.

The application of identifying this phenomenon in time series data for thin layer detection requires further synthetic testing. First, the effect of designing layer stacks with small perturbations in thickness or velocity should be addressed in terms of variation in mean frequency and bandwidth of the reflected energy spectrum. Experiments can also be designed to determine whether the superposition of multiple periodicities can be resolved by this technique. In addition, the layer stack model can be extended to two dimensions where additional information may be derived from offset recording.

Chapter 6

Object-based stochastic facies inversion

6.1 Introduction

Reservoir models are a necessary tool during the exploration, delineation, and exploitation of hydrocarbon reservoirs. Data quality and resolving power are often too limited to build a detailed, deterministic model where all heterogeneity was fully observed in the data. Instead, stochastic methods are used to fill in unresolved details at short scales (e.g. Dubrule, 1989; Haas and Dubrule, 1994). The stochastic nature of these models allows construction of different realizations which all have the same broad characteristics but differ in the details. These differences qualify and quantify the uncertainty and risk related to the incomplete knowledge and sparse data coverage. Such realizations may be generated by defining a model and specifying its parameters which encompass composition and internal structure of the reservoir.

Core and geophysical wireline data provide a detailed account of the lithologic composition of a reservoir and are capable of identifying small-scale heterogeneities at the well

locations. These data are incapable of resolving features that deviate from the well path. Their lateral extents, for example, are unresolved, and hence, log correlation and deterministic seismic interpretations are often used to interpolate between wells.

The seismic reflection interpretations provide a means of resolving lateral and vertical heterogeneity between wells, but are subject to a vertical resolution limit of $\frac{1}{4}$ wavelength and a lateral limit of one Fresnel zone ($\approx \sqrt{\text{depth} \cdot \text{wavelength}}$). Due to resolution limits of deterministic seismic interpretations, and the one dimensional nature of core and wireline data, conventional techniques of generating reservoir models rely on experience, geologic intuition, and modern environments or ancient outcrop analogs to further characterize a reservoir. For example, to characterize a reservoir exhibiting channelized features, intuition and analogs aid in defining the sinuosity of small-scale channels, width-to-depth ratios of associated facies, and how these associated facies are positioned spatially with respect to one another.

Object-based reservoir models build a realization by emplacing geologically meaningful geometric shapes representing channels, barriers, and other geologic objects using geometric and stochastic parameters such as distributions of thickness, sinuosity and/or aspect ratio. The purpose of the proposed object-based stochastic facies inversion is to reduce the dependence on geologic intuition and analogs when generating realizations of hydrocarbon reservoirs.

I outline a pilot study technique which estimates model parameters and their distributions and ranges from all available data, including plentiful seismic attributes. The inversion process begins with an initial reservoir realization, which is compared to observed data. Based on this comparison, a new set of parameters is chosen. The new set of parameters is used in the object-based reservoir simulation to generate a new realization, which is conditioned to the well logs. This iterative process continues until a single model with a user defined "acceptable" match between the realization and data is attained.

The inversion is highly nonlinear, and hence, convergence cannot be taken for granted and may be excruciatingly slow. We also have to emphasize that this contribution is only a first outline of such a procedure. Many questions remain unresolved and will need to be resolved later. For example, which seismic attributes should be used: amplitudes, impedance, or something else? Should seismic attributes be used for both the conditioning of realizations and the improvement of parameters? We believe, however, that the outlined quantitative approach to the definition of these parameters will generate reservoir models with improved realism and increased correlation between predicted and recorded production histories.

6.2 Process

Our technique for generating a reservoir realization is contained in two loops as depicted in the schematic diagram shown on Figure 6.1. In the outer loop (shown in blue), we optimize the set of model parameters. In the inner loop (shown in red), we optimize the realization for a given set of parameters. In fact, we are searching for the set of random numbers which yields the stochastic model realization most compatible with the constraining wireline and seismic data!

The inner loop consists of generating an object based realization. For simplicity, we use the industry standard RMS composite facies module by Roxar (2002), although competing or homegrown software modules would perform equally well. The objects are distributed in accordance to specified volumetric proportions, statistical distributions for the parameters, and placement rules which govern clustering. The generated models honor a set of interval facies logs. They are also constrained by external seismic attributes. The volumetric proportion of the facies are simply estimated by the linear footage of the facies present in the logs. Placement rules are suggested by the environment and the geologic interpretation of the geometric shapes. The software module simply adds objects into the volume. Location,

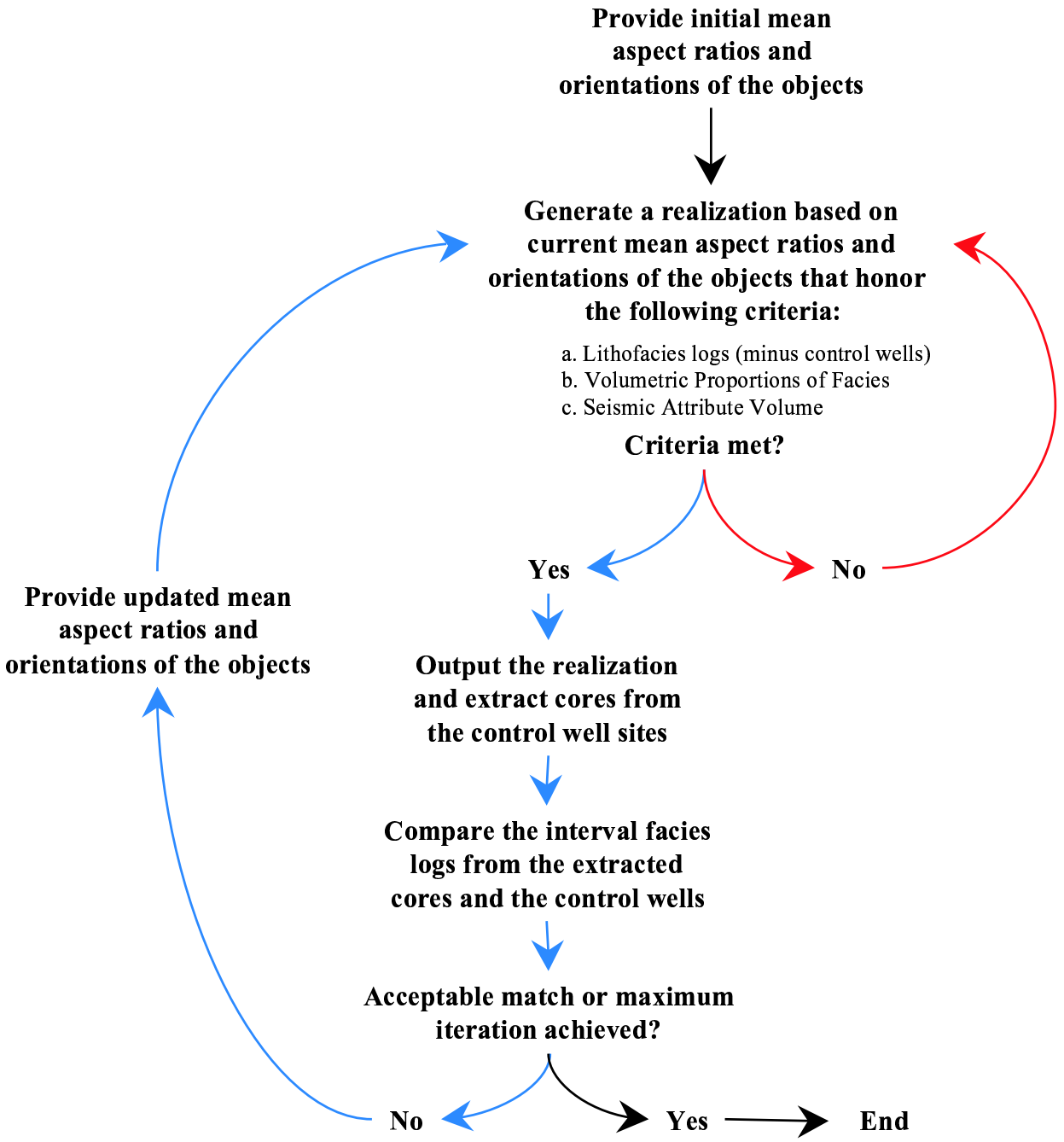

Figure 6.1: Schematic depicting the object-based stochastic facies inversion depicting the inner (red) and outer (blue) loops

.

orientation, and other geometric parameters are drawn from the specified distributions. A placed object which is incompatible with the wireline or seismic constraints is simply removed again. The module tries adding objects until the specified volumetric proportions are satisfied within some predefined tolerance interval. Once completed, the process advances to the outer loop with the single realization that passed these criteria. Because the module tries to condition its realizations perfectly to the wells, a portion of all available wells are excluded from use in the inner loop for exclusive use in the outer loop.

The outer loop optimizes the geometrical parameters such as aspect ratios and orientations of the included geologic objects. The optimization of these parameters is achieved via a simulated annealing (SA) guided search technique to nonlinear inversion. The inversion model space m_{rs} is populated with the statistical parameters necessary to generate a reservoir realization,

$$\mathbf{m} = \begin{bmatrix} m_{1,1} & m_{2,1} & \cdots & m_{R-1,1} & m_{R,1} \\ m_{1,2} & m_{2,2} & \cdots & m_{R-1,2} & m_{R,2} \\ \vdots & \vdots & \ddots & \vdots & \vdots \\ m_{1,S-1} & m_{2,S-1} & \cdots & m_{R-1,S-1} & m_{R,S} \\ m_{1,S} & m_{2,S} & \cdots & m_{R-1,S} & m_{R,S} \end{bmatrix} \tag{6.1}$$

modified from Sen and Stoffa (1991), where each row (1 through S) corresponds to a particular statistical parameter and each column (1 through R) corresponds to a possible value that the respective parameter can attain. For instance, $m_{1\rightarrow R,1}$ may correspond to R possible values for mean channel width, $m_{1\rightarrow R,2}$ may correspond to the R possible standard deviations associated with that mean channel width, etc.

After the initial model was chosen $m_{1,1\rightarrow S}$ and a realization generated, cores are extracted from the realization C_s at the location of the omitted interval facies logs C_o. This ensemble of omitted logs serves as the observed data to calculate the objective function. The binary

objective function E is evaluated such that if $C_o(x,y,z) = C_s(x,y,z)$ then $e = e+1$, however if $C_o(x,y,z) \neq C_s(x,y,z)$ then $e = e+0$ and $E = \frac{e}{z_{\text{total}}}$.

This process repeats for all R values of the current parameter, maintaining constant values for $m_{1,2\rightarrow S}$. A probability distribution P

$$P(m_{rs}) = \frac{\exp(\frac{E(m_{rs})}{T})}{\sum_{r=1}^{R}\exp(\frac{E(m_{rs}}{T})} \text{ where } T = T_0 * 0.99^i \tag{6.2}$$

is evaluated (Sen and Stoffa, 1991), which calculates the likelihood that any one of the R values of the current parameter is correct based on the energy function E.

A new value for the current parameter is retained based on this probability distribution and the process continues to the next parameter, maintaining constant values for parameters $m_{r,1}$ and $m_{1,3\rightarrow S}$. An iteration i in the annealing process constitutes the completion of evaluating the R^{th} value of the S^{th} parameter, the temperature T is lowered, and the cycle repeats until the user defined "acceptable" match between the observed and synthesized log data is attained. To establish a computationally efficient cooling process, experimental trials are often performed before selecting the initial temperature T_0.

6.3 Application to the Coalinga heavy oil field

Our novel method of generating reservoir realizations is applied to ChevronTexaco's Coalinga heavy oil field in the San Joaquin Valley of southwestern California, shown on Figure 6.2. The Coalinga field is a mature field with an abundance of wireline log data which makes this an ideal site to test our methodology. For this project, we used 106 wells spread over 3 square miles, shown in Figure 6.3, which allowed exclusion of a generous number of wells to be used solely for evaluation of the objective function E.

The Coalinga field has been producing oil from the Temblor formation since 1887 (Clark

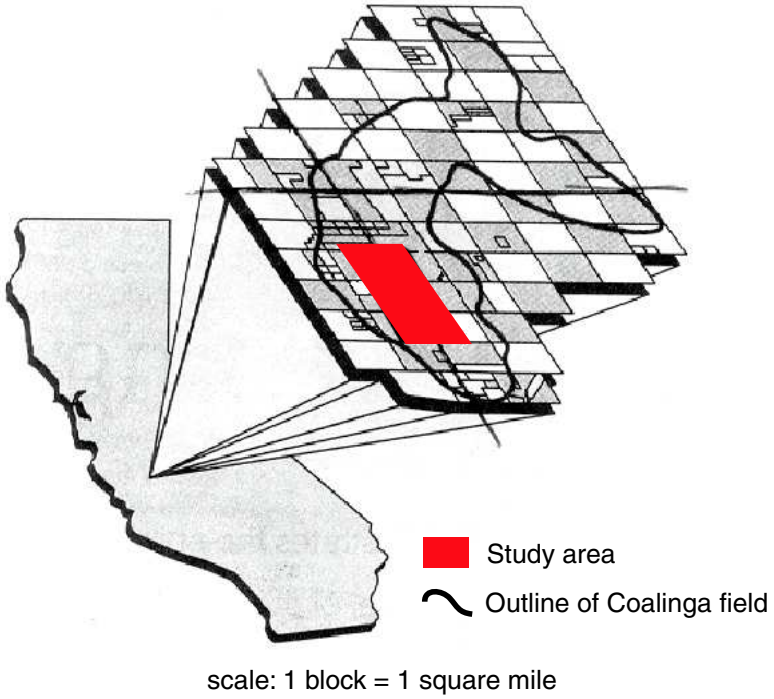

Figure 6.2: Location of the Coalinga oil field in southwestern California.

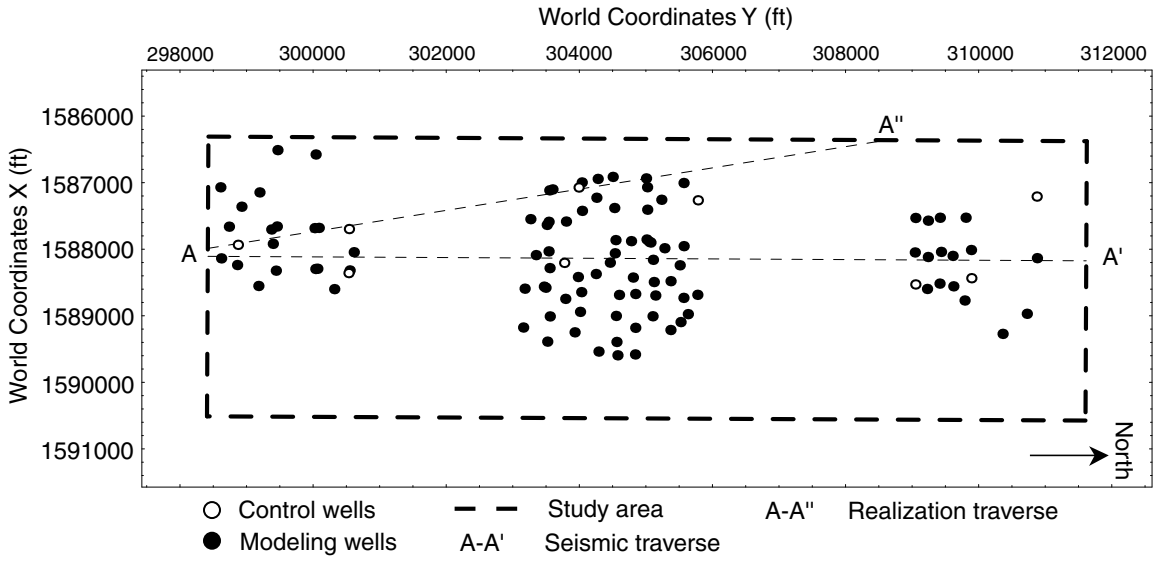

Figure 6.3: Map showing the location of the modeling and control wells, the seismic line shown in Figure 6.4, and the cross section through the realizations shown in Figure 6.6.

et al., 2001). Based on the characterization by Clark et al. (2001), the Temblor formation is an unconformity bounded reservoir and can be subdivided into three main depositional zones as shown on Figure 6.4. The basal zone is bounded at the base by a major erosional surface, Base Temblor, which is identified on seismic data by the truncated marine shales of the underlying Kreyenhagen formation. This section is largely estuarine facies consisting of tidal channel and stacked tidal channels deposits (Clark et al., 2001). The Buttonbed unconformity marks the transition from the estuarine deposits to tide and wave dominated shoreline facies. This middle section, primarily composed of prograding units of coarsening-upward sandstones (Clark et al., 2001), is in turn capped by the Valv unconformity. This unconformity defines the transition to subtidal dominated facies consisting of cemented, laterally continuous, coarsening-upward sandstones (Clark et al., 2001), which is bounded at the top by the Top Temblor.

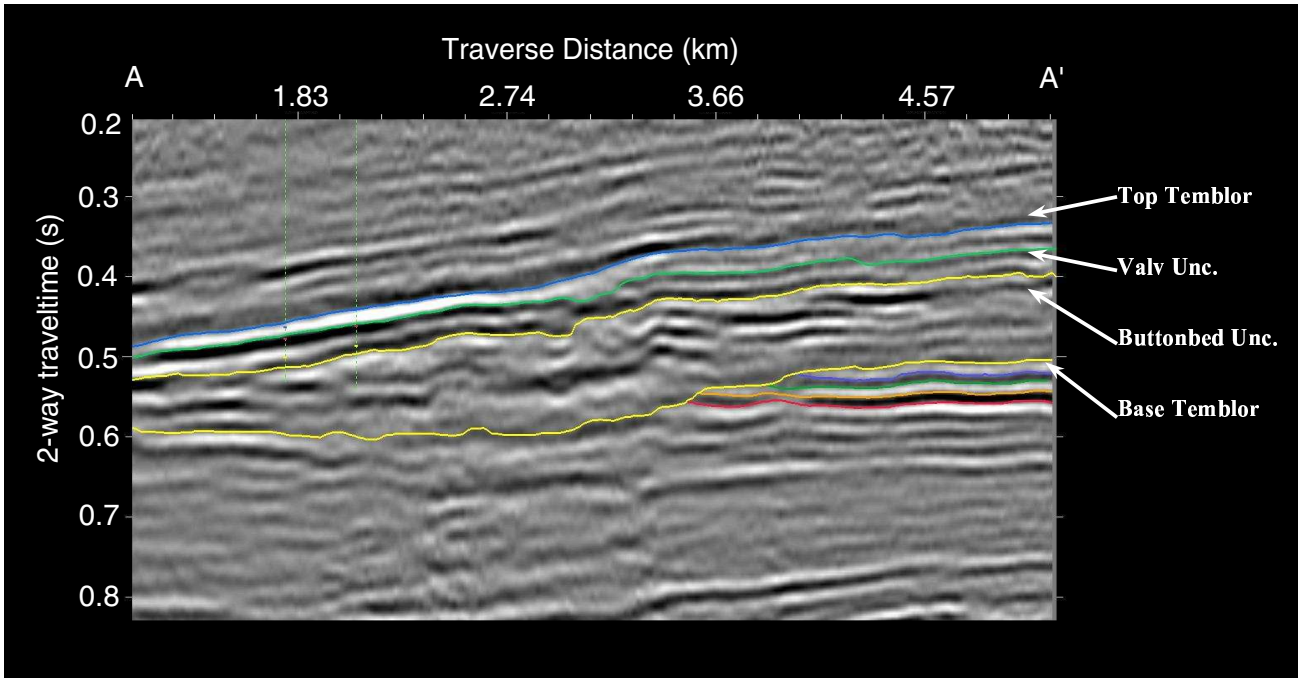

Figure 6.4: Dominant stratigraphic intervals within the Temblor formation

Table 6.1: Parameters and ranges for the basal zone of the Temblor formation. The dominant laminated sand, silt, and shale group is used as background into which other lithologies are embedded.

Lithofacies Group	Index Number	Volume Fraction (-)	Mean Length (m)	Mean Width (m)	Mean Thickness (ms)	Orientation (°)
Sand	1	0.085	36.5 – 91.4	36.5 – 91.4	3.0 – 8.5	0 – 90
Laminated Sand, Silt and Shale	2	0.497	NA	NA	NA	NA
Burrowed Clay	3	0.147	36.5 – 204.2	36.5 – 204.2	3.0 – 16.8	0 – 90
Burrowed Sand	4	0.196	36.5 – 204.2	36.5 – 204.2	3.0 – 16.8	0 – 90
Fossiliferous Sand and Clay	5	0.058	36.5 – 64.0	36.5 – 64.0	3.0 – 5.8	0 – 90
Limestone	6	0.015	36.5	36.5	3.0	0
Calcareous Cemented Sand	7	0.002	36.5	36.5	3.0	0

Currently, production is focused in the basal zone of the Temblor formation and is aided by steam injection. Based on the wireline log interpretations of Mize (2002) and Piver (2004), seven lithofacies types occur in this basal zone of the Temblor formation and are listed in Table 6.1.

Because the laminated sand, silt and shale are the dominant facies in this zone at 49.7%, they are treated as the background material, where the other facies types are emplaced during the reservoir modeling. The remaining six lithofacies are modeled as arbitrary rectangular prisms with the ranges of aspect ratios and orientations specified in Table 6.1. Due to the relatively rare occurrence of limestone and calcareous cemented sand ($< 2\%$), the aspect ratios are kept constant and small to prevent instabilities in generating a realization. In addition, the standard deviations associated with these aspect ratios and orientations remained fixed at 20% their respective mean value.

For this example, we chose a seismo-facies volume as the seismic attribute to condition the reservoir modeling. This volume is calculated by the multiple regression analysis tool in the Emerge module of the Hampson Russell (2000) software package. The Emerge module provides a means to predict a core or well attribute, in this case interval facies, at the seismic trace location from any combination and number of seismic attributes (e.g. Tanner, 1978). The step-wise process first determines the best single seismic attribute discriminator of the well attribute, then finds by trial-and-error the best pair of seismic attributes given that one of the pair is the best single seismic attribute, and then the best three, four, etc. In this case we chose the following eight seismic attributes to predict the interval facies logs at the seismic trace locations: LOG[impedance], integrated absolute amplitude, integrate, instantaneous response frequency, instantaneous dominate frequency, quadrature trace, perigram^2, and instantaneous amplitude^{-1}.

Due to time considerations, the inversion process was allowed to run for nine iterations ($\approx$ 168 hours continuous CPU time) and achieved a 51% match between the nine omitted interval facies logs C_o and the cores extracted from the final single realization C_s. As depicted on the convergence plot shown on Figure 6.5, this represents a 19% improvement from the initial 32% match between the control logs and the cores extracted from the initial single realization. The statistical parameters used to generate this final realization are listed in Table 6.2.

Figure 6.6, shown as a function of traverse distance and two-way traveltime below the interpreted Buttonbed unconformity, depicts a cross-section through the initial and final realization intersecting three of the omitted control wells. The extracted and omitted interval facies logs from these well locations are enlarged and depicted in Figure 6.7. The match between the control logs and those extracted from the initial realization (Figures 6.7(a), 6.7(b) and 6.7(c)) is marginal at best, however after nine iterations the extracted logs (Figures 6.7(d), 6.7(e) and 6.7(f)) are strikingly similar to the control logs. These results merely

Table 6.2: Parameters used to generate a realization for the basal zone of the Temblor formation with 51% agreement between the control and extracted interval facies logs. The dominant laminated sand, silt, and shale group is used as background into which other lithologies are embedded.

Lithofacies Group	Index Number	Mean Length (m)	Mean Width (m)	Mean Thickness (ms)	Orientation (°)
Sand	1	36.5	36.5	8.5	30
Laminated Sand, Silt and Shale	2	NA	NA	NA	NA
Burrowed Clay	3	82.3	189.0	12.2	70
Burrowed Sand	4	51.8	189.0	3.0	90
Fossiliferous Sand and Clay	5	51.8	51.8	5.2	70
Limestone	6	36.5	36.5	3.0	0
Calcareous Cemented Sand	7	36.5	36.5	3.0	0

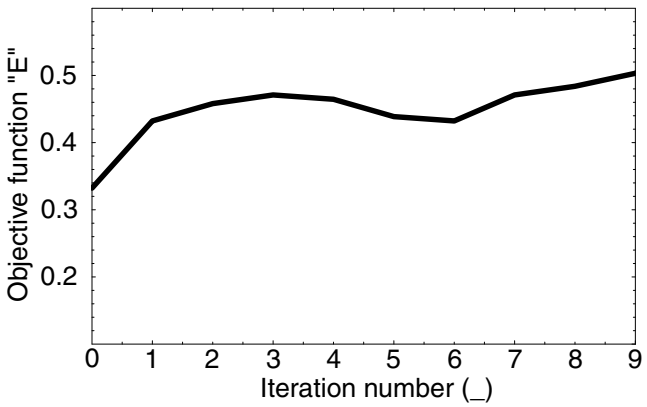

Figure 6.5: Depicts the convergence of the inversion (correlation verses iteration) from 32% to 51% in nine iterations based on nine control wells

emphasize the significance of a 19% improved correlation between the facies interpretations at the control points and synthesized data.

6.4 Discussion and Conclusions

The adaptation to conventional techniques of generating reservoir models consists of using a simulated annealing parameter optimization technique as a proxy to geologic intuition and analogs. The results of this study suggest that a more systematic and quantitative approach to defining the statistical model parameters necessary to generate reservoir models is possible and can improve the match between predicted models and observed data. The recovery of these parameters that define the composition and internal short-scale structure of a reservoir through this formulation aids in resolving inter-well and possibly inter-trace heterogeneity.

This improvement, however, comes at a high computational expense. One iteration requires evaluation of $R \times S$ forward models. For this study with $S = 16$ parameters and $R = 10$ possible values that each parameter can attain, one complete iteration typically required approximately 24 hrs of continuous CPU time on a SUN Blade 1000 workstation

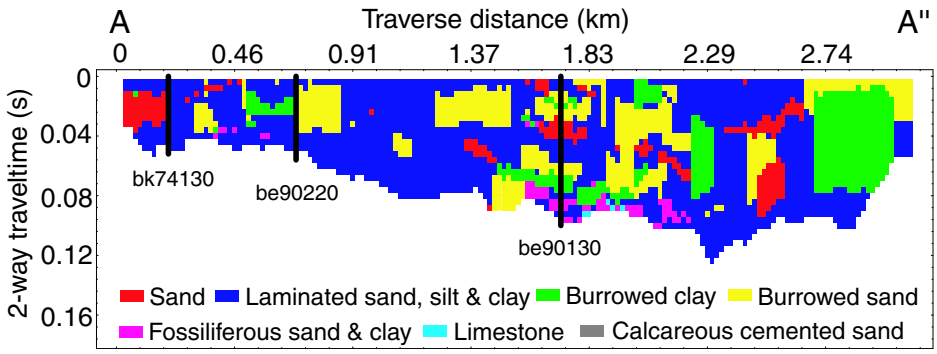

(a)

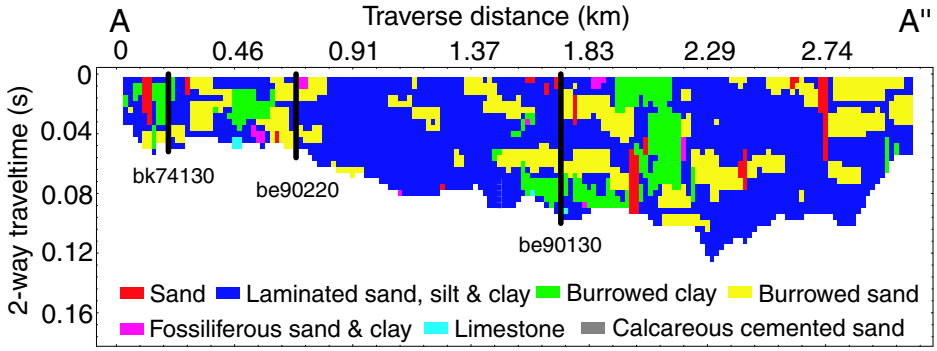

(b)

Figure 6.6: Cross-section, through **(a)** the initial and **(b)** final realizations, intersecting three control wells.

with a single 500 MHz processor. Different models, however, could be evaluated in parallel on a grid computer or parallel cluster which would reduce the required computer time linearly with the number of parallel evaluations. We did not have the necessary number of licenses for the object-based modeling software to explore this time saving strategy.

I presented just a pilot implementation of our proposed modeling technique. Some changes may be warranted for future applications. For example, excluding a different set of boreholes to evaluate the outer loop (Figure 6.1) during every iteration which resembles jackknifing often used for statistical testing with limited data (e.g., Efron, 1982), may improve our confidence in the final realization. Also, we would like to use seismic data not only in the inner loop (Figure 6.1) as a constraint for the object-based model, but also in

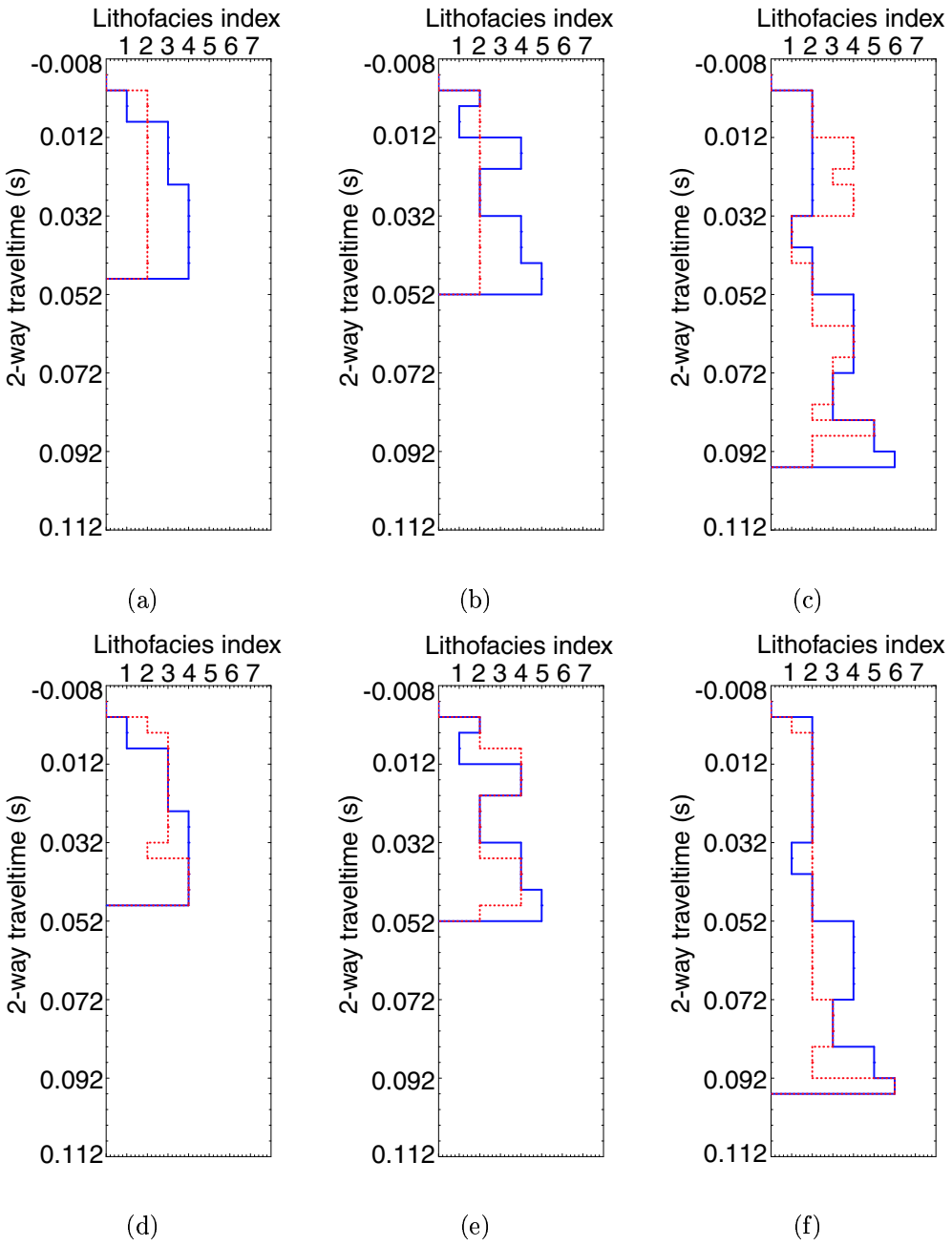

Figure 6.7: Enlarged view of the control (Blue) and extracted (Red) interval facies logs from the **(a)** bk74130, **(b)** be90220 and **(c)** be90130 well locations for the initial realization and **(e)** bk74130, **(f)** be90220 and **(g)** be90130 well locations for the final realization.

the outer loop to evaluate the objective function E. Currently, parameter optimization is performed with only a small amount of data. Seismic data volumes would have a dramatic impact on this optimization. The simulated annealing procedure was used in its discrete

form where parameters can take only discrete values. There are continuous versions of simulated annealing as well as other nonlinear inversion algorithms, such as the genetic algorithm (Stoffa and Sen, 1991) and neighbourhood algorithm (Sambridge, 1999), which may improve performance. Lastly, the performance of the proposed scheme should be evaluated with truly independent data instead of convergence or correlation criteria. One potential assessment would be to subject the reservoir models to flow simulations to compare predicted and recorded production histories.

There are also some unresolved research questions. The most pressing one is which seismic data to use in the inner and outer loops. For the inner loop, any seismic attribute could be used as a modeling constraint. Some attributes, however, may perform better while others may have a direct physical or petrophysical meaning. At present, it is not clear which attributes to select. For the use of seismic data in the outer loop, we have to transfer either the realizations, the seismic data, or both to one common quantity. For example, we could transform the realization to an impedance volume, and apply the convolutional model with an appropriate wavelet to obtain synthetic traces for comparison with the seismic amplitude data. Instead of directly comparing amplitudes, maybe one should compare seismic attributes of the synthetic and real data. As an alternative, we could invert the real seismic data into an acoustic impedance volume with the help of wireline data, and compare the resulting impedance volume estimate with the impedance of the model realization. And of course there may be other ways of comparing seismic data and model realizations.

Despite the obvious potential for improvements and the unresolved research questions, we believe that the outlined approach can eventually generate reservoir models with improved realism, better predictions and improved matches against control data, and better agreement between predicted and recorded production data.

Appendix A

Radon Transform

When processing offset recorded seismic data, the Radon transform maps events exhibiting a linear, parabolic, or hyperbolic trajectory in offset verses traveltime data (i.e. Figures A.1(a), A.1(b), and A.1(c)) to individual events in the moveout (or deviation in traveltime from zero offset to maximum offset) verses traveltime domain (Figures A.1(d), A.1(e), and A.1(f)), and vice versa.

After taking the temporal Fourier transform of each moveout trace, the inverse Radon transform can be posed as the least-squares problem $\mathbf{d} = \mathbf{Gm}$. For a constant angular frequency ω, the vectors $\mathbf{d}$ and $\mathbf{m}$ correspond to the offset x dependent data and the moveout p dependent model. These vectors are related by the Radon operator matrix $\mathbf{G} = \exp[-i\omega p\theta(x)]$. This function $\theta(x)$ controls how the events in the data are mapped to the model space and vice versa. For instance, $\theta(x) = \frac{x}{x_{\max}}$, $\frac{x^2}{x_{\max}^2}$, or $\frac{1}{x_{\max}}(\sqrt{x^2 + z_{\text{ref}}^2} - z_{\text{ref}})$ for linear, parabolic or hyperbolic transformations (Bickel, 2000), where $x_{\max}$ denotes the maximum offset x and z_{ref} refers to a user defined reference depth. When this inversion is performed for all frequencies the result is an offset verses frequency domain. The inverse Fourier transform calculated at each offset produces the offset verses traveltime data.

Because the inverse transform has been initially cast as a least-squares problem, three

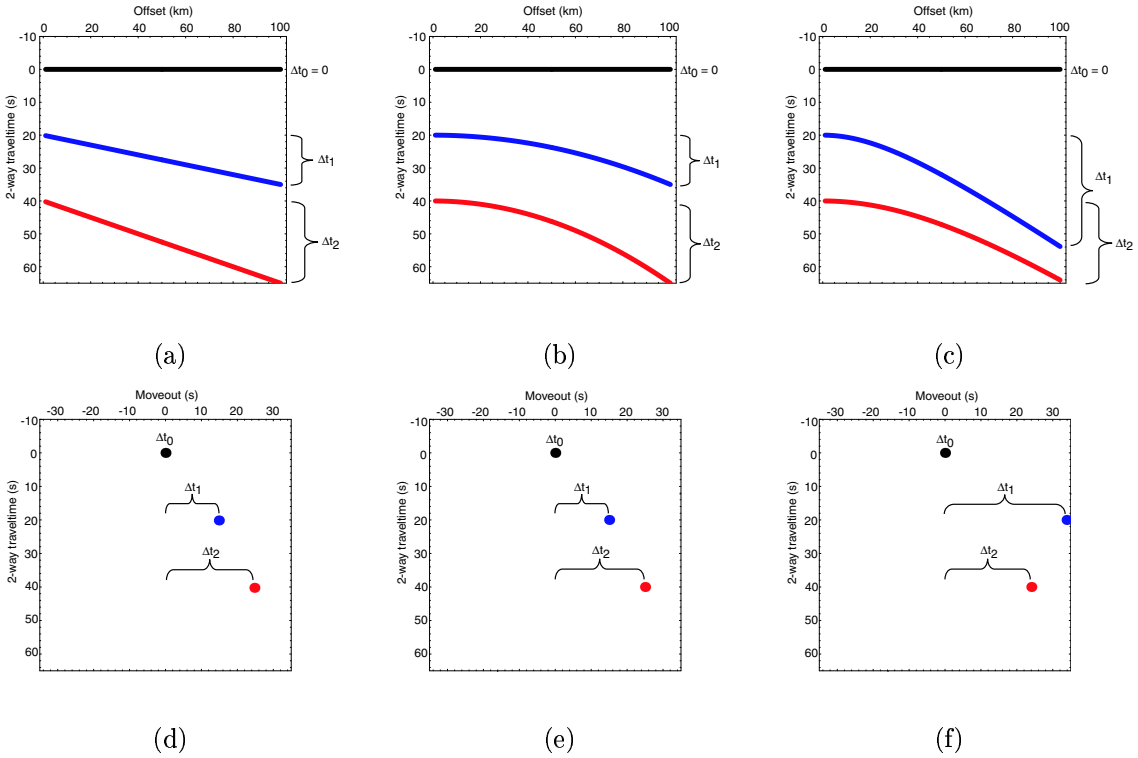

Figure A.1: Depicting **(a)** linear, **(b)** parabolic, and **(c)** hyperbolic events in the offset verses traveltime domain and **(d)** the linear transform of **(a)**, **(e)** the parabolic transform of **(b)**, and **(f)** the hyperbolic transform of **(c)**.

possible solutions exist for the forward transform, namely, an over-, under-, and mixed-determined solution. The over determined problem describes the situation where there are more linearly independent data parameters than model parameters. The solution to this problem follows from minimizing the data misfit $\mathbf{e} = \mathbf{d} - \mathbf{Gm}$ such that $\frac{\partial}{\partial m_q}\mathbf{e^T e} = 0$. In practice, however, this situation rarely occurs because the forward transform is typically performed over a greater number of moveouts than offsets. In addition, the data parameters may be linearly dependent suggesting a rank-deficient, slightly under determined or mixed determined problem. The solution to this mixed-determined problem comes by the way of minimizing the misfit subject to the weighted damped model size

$$\phi(\mathbf{m}) = \mathbf{e^T e} + \epsilon \mathbf{m^T W m}. \tag{A.1}$$

Here ϵ, the damping factor, controls the trade-off between prediction error (data misfit) and solution error (model size) and $\mathbf{W}$ refers to a diagonalized weighting matrix containing some *a priori* information about the inverse problem. By rewriting (A.1) in indicial notation

$$\phi(\mathbf{m}) = \sum_{i}^{N} (d_i - \sum_{j}^{M} G_{ij} m_j)(d_i - \sum_{k}^{M} G_{ik} m_k) + \epsilon \sum_{k}^{M} W_{kk} m_k^2 \tag{A.2}$$

and $\frac{\partial \phi(\mathbf{m})}{\partial m_q} = 0$ leads to the weighted damped least squares solution to $\mathbf{Gm} = \mathbf{d}$,

$$\mathbf{m^{est}} = (\mathbf{W^{-1}G^H G} + \epsilon \mathbf{I})^{-1} \mathbf{W^{-1}G^H d}, \tag{A.3}$$

after Menke (1989). Here, the $\mathbf{G^H}$ denotes the adjoint or conjugate transpose of the operator matrix $\mathbf{G}$, and $\mathbf{I}$ refers to the identity matrix. At this point, a distinction can be made between conventional Radon transforms $W_{ii} = I_{ii}$ and high resolution Radon transforms $W_{ii} \neq I_{ii}$ for the mixed-determined solution. We chose the continuity preserving weighting matrix described in Herrmann et al. (2000) such that for $k = 1$, $W_{ii}^{-1}(\omega_k) = I_{ii}$ and $k > 1$, $W_{ii}^{-1}(\omega_k) = \text{abs}[m_i^{\text{est}}(\omega_{k-1})]$, where the absolute value of the model $\mathbf{m^{est}}$ calculated at the preivious frequency ω_{k-1} occupies the diagonal elements of the weighting matrix $\mathbf{W^{-1}}$ for the current frequency ω_k.

In this case, the damping factor ϵ consists of an experimentally defined prewhitening factor α and an approximation to the operators condition number

$$\epsilon = \alpha \frac{(\sum_j^M (\mathbf{W^{-1}G^H G})_{1j})^2}{\sum_j^M (\mathbf{W^{-1}G^H G})_{1j}^2}. \tag{A.4}$$

The forward Radon transform can be calculated by taking the Fourier transform of each offset trace, evaluating equation A.2 at each frequency, and taking the inverse Fourier transform of each moveout trace.

Appendix B

Summary of calculations

The seismic waves modeled by a 1-D space-time finite difference approximation to the scalar wave equation can written as

$$\frac{d^2}{dx^2}U\left(x,t\right)-\frac{1}{c(x)}\frac{d^2}{dt^2}U\left(x,t\right)+S\left(x,t\right)=0, \tag{B.1}$$

where $c(x)$ is acoustic velocity, $U(x,t)$ refers to a displacement-time function, and $S(x,t)$ denotes a source-time function all located at x. The wave equation can be discretized using spatial and temporal steps h and k:

$$\frac{1}{h^2}\left(U_{i-1}^n-2U_i^n+U_{i+1}^n\right)-\frac{1}{k^2c_i^2}\left(U_i^{n-1}-2U_i^n+U_i^{n+1}\right)+S_i^n=0, \tag{B.2}$$

where U_i^n denotes $U(x=ih,t=nk)$ and S_i^n is give by a Ricker wavelet acting at a constant spatial position i_c

$$S_{i_c}^n=\left\{1-2\pi^2f_c^2(nk-t_s)^2\right\}e^{-\pi^2(nk-ts)^2f_c^2}, \tag{B.3}$$

where f_c is the center frequency and t_s is a time shift typically greater than $\frac{1}{f_c}$ to enforce

causality modified from Sheriff and Geldart (1995). If U^{n-1} and U^n are known U^{n+1} can be predicted by:

$$U_i^{n+1} = \left(\frac{c_i k}{h}\right)^2 \left(U_{i-1}^n - 2U_i^n + U_{i+1}^n\right) + \left(2U_i^n - U_i^{n-1}\right) + \left(S_i^n - S_i^{n-1}\right). \tag{B.4}$$

Note that for stability reasons $\frac{c_i k}{h} < 1$ (Jensen et al., 1994). By extending B.1 to accommodate wave propagation in two dimensions the 2-D space-time finite difference approximation to the wave equation can be written as

$$U_{i,j}^{n+1} = \left(\frac{c_{i,j} k}{h}\right)^2 \left(U_{i-1,j}^n + U_{i+1,j}^n + U_{i,j-1}^n + U_{i,j+1}^n - 4U_{i,j}^n\right) + \left(2U_{i,j}^n - U_{i,j}^{n-1}\right) + \left(S_{i,j}^n - S_{i,j}^{n-1}\right). \tag{B.5}$$

For any $f(t)$ the frequency representation $F(\omega)$ can be calculated by the forward Fourier transform

$$F(\omega) = \int f(t) e^{i\omega t} dt, \tag{B.6}$$

the energy spectrum is calculated by

$$E(\omega) = |F(\omega)|^2 = F(\omega) F^*(\omega), \tag{B.7}$$

where $*$ denotes complex conjugate. From equation (B.7), the mean frequency

$$\overline{\omega} = \int \omega E(\omega) d\omega \tag{B.8}$$

and bandwidth

$$B^2 = \int (\omega - \overline{\omega})^2 E(\omega) d\omega \tag{B.9}$$

can be calculated (Cohen, 1995).

Bibliography

N. C. Banik, I. Lerche, J. R. Resnick, and R. T. Shuey. Stratigraphic filtering, part 2: Model spectra. *Geophysics*, 50:2775–2783, 1985a.

N. C. Banik, I. Lerche, and R. T. Shuey. Stratigraphic filtering, part 1: Derivation of the O'Doherty-Anstey formula. *Geophysics*, 50:2768–2774, 1985b.

R. Bansal and M. Imhof. Diffraction enhancement in prestack seismic data. *Geophysics*, 2004. in press.

S. H. Bickel. Focusing aspects of the hyperbolic radon transform. *Geophysics*, 65:652–655, 2000.

M. S. Clark, L. F. Klonsky, and K. E. Tucker. Geologic study and multiple 3-D surveys give clues to complex reservoir architecture of giant Coalinga oil field, San Joaquin Valley, California. *Leading Edge*, pages 774–751, 2001.

L. Cohen. *Time–Frequency Analysis*. Prentice Hall, Englewood Cliffs, New Jersey, 1995.

T. M. Daley, K. T. Nihei, L. R. Myer, E. L. Majer, J. H. Queen, M. Fortuna, and J. Murphy. Numerical modeling of scattering from discrete fracture zones in a San Juan basin gas reservoir. *SEG Expanded Abstracts*, pages 109–112, 2002.

H. L. Deng. Acoustic wave propagation in thin layered media with steep reflectors. *Geophysics*, 59:1593–1604, 1994.

O. Dubrule. A review of stochastic models for petroleum reservoirs. *Geostatistics*, 2:493–506, 1989.

B. Efron. *The jackknife, the bootstrap, and other resampling plans.* Society for Industrial and Applied Math, Philadelphia, Pennsylvania, 1982.

D. J. Foster and C. C. Mosher. Suppression of multiple reflections using the radon transform. *Geophysics*, 57:386–395, 1992.

A. Haas and O. Dubrule. Geostatistical inversion-a sequential method of stochastic reservoir modeling constrained by seismic data. *First Break*, 12:561–569, 1994.

Hampson Russell. *Hampson Russell Earth Imaging Solutions, Installation and Tutorials.* Hampson-Russell Software Services, Calgary, Canada, 2000.

P. Herrmann, T. Mojesky, and P. Hugonnet. De-aliased high-resolution Radon transforms. *SEG Expanded Abstracts*, pages 1953–1956, 2000.

M. G. Imhof. Scale dependence of reflection and transmission coefficients. *Geophysics*, 68: 322–336, 2003.

F. B. Jensen, W. A. Kuperman, M. B. Porter, and H. Schmidt. *Computational Ocean Acoustics.* American Institute of Physics, Woodbury, New York, 1994.

M. M. N. Kabir and K. J. Marfurt. Toward true amplitude multiple removal. *The Leading Edge*, pages 66–73, 1999.

W. Menke. *Geophysical Data Analysis: Discrete Inverse Theory.* Academic Press, San Diego, California, 1989.

K. L. Mize. Development of three-dimensional geological modeling methods using cores and geophysical logs, West Coalinga field, California. Master's thesis, Clemson University, 2002.

R. F. O'Doherty and N. A. Anstey. Refections on amplitudes. *Geophysical Prosecting*, 55: 1158–1165, 1971.

J. L. Piver. Integration of geologic models and seismic data to characterize interwell heterogeneity of the miocene Temblor formation, Coalinga, California. Master's thesis, Clemson University, 2004.

Roxar. *RMS users guide.* Roxar RMS, Stavanger, Norway, 2002.

E. Saenger, S. Shapiro, and O. Kruger. Simultation of the diffraction by single cracks: An accuracy study. *SEG Expanded Abstracts*, pages 2007–2010, 2002.

M. Sambridge. Geophysical inversion with a neighbourhood algorithm I. Searching a parameter space. *Geophys. J. Int.*, pages 479–494, 1999.

M. K. Sen and P. L. Stoffa. Nonlinear one-dimensional seismic waveform inversion using simulated annealing. *Geophysics*, 56:1624–1638, 1991.

P. Sheng. *Introduction to Wave Scattering, Localization, and Mesoscopic Phenomena.* Academic Press, Inc, San Diego, California, 1995.

R. E. Sheriff and L. P. Geldart. *Exploration Seismology.* Cambridge University Press, New York, New York, 1995.

P. L. Stoffa and M. K. Sen. Nonlinear multiparameter optimization using genetic algorithms: Inversion of plane-wave seismograms. *Geophysics*, 56:1794–1810, 1991.

M. T. Tanner. Complex seismic trace analysis. *Geophysics*, 44:1041–1063, 1978.

D. Trad, T. Ulrych, and M. Sacchi. Latest views of the sparse Radon transform. *Geophysics*, 68:386–399, 2003.

R. Verm and F. Hilterman. Lithology color-coded seismic sections: The calibration of AVO crossplotting to rock properties. *The Leading Edge*, pages 847–853, 1995.

M. R. J. Wyllie, A. R. Gregory, and G. H. F. Gardner. An experimental investigation of factors affecting elastic wave velocities in porous media. *Geophysics*, 23:459–493, 1957.